Metabolic reprogramming of cancer cells by JMJD6-mediated pre-mRNA splicing is associated with therapeutic response to splicing inhibitor

Carolyn Jablonowski[1#], Waise Quarni[1#], Shivendra Singh[1], Haiyan Tan[2], Dhanushka Hewa Bostanthirige[1], Hongjian Jin[3], Jie Fang[1], Ti-Cheng Chang[2], David Finkelstein[3], Ji-Hoon Cho[2], Dongli Hu[1], Vishwajeeth Pagala[2], Sadie Miki Sakurada[4], Shondra M. Pruett-Miller[4], Ruoning Wang[5], Andrew Murphy[1], Kevin Freeman[6], Junmin Peng[2,9], Andrew M Davidoff[1,7,8], Gang Wu[3], Jun Yang[1,7,8, 9]

[1]Department of Surgery, St Jude Children's Research Hospital, Memphis, TN38105, USA

[2]Center for Proteomics and Metabolomics, Department of Structural Biology, Department of Developmental Neurobiology, St Jude Children's Research Hospital, Memphis, TN38105, USA

[3]Center for Applied Bioinformatics, St Jude Children's Research Hospital, Memphis, TN38105, USA

[4]Department of Cell and Molecular Biology, St. Jude Children's Research Hospital, Memphis, TN 38105, USA.

[5]Center for Childhood Cancer and Blood Disease, Abigail Wexner Research Institute, Nationwide Children's Hospital, 700 Children's Drive, Columbus, OH 43205, USA.

[6]Genetics, Genomics & Informatics, The University of Tennessee Health Science Center (UTHSC), Memphis, TN 38103, USA.

[7]St Jude Graduate School of Biomedical Sciences, St Jude Children's Research Hospital, TN 38105

[8]Department of Pathology, College of Medicine, The University of Tennessee Health Science Center, 930 Madison Ave, Suite 500, Memphis, TN 38163

#equal contribution

[9]Correspondence: Jun.Yang2@stjude.org

The authors declare no potential conflicts of interest

Abstract

Dysregulated pre-mRNA splicing and metabolism are two hallmarks of MYC-driven cancers. Pharmacological inhibition of both processes has been extensively investigated as potential therapeutic avenues in preclinical and clinical studies. However, how pre-mRNA splicing and metabolism are orchestrated in response to oncogenic stress and therapies is poorly understood. Here, we demonstrate that JMJD6 acts as a hub connecting splicing and metabolism in MYC-driven neuroblastoma. JMJD6 cooperates with MYC in cellular transformation by physically interacting with RNA binding proteins involved in pre-mRNA splicing and protein homeostasis. Notably, JMJD6 controls the alternative splicing of two isoforms of glutaminase (GLS), namely kidney-type glutaminase (KGA) and glutaminase C (GAC), which are rate-limiting enzymes of glutaminolysis in the central carbon metabolism in neuroblastoma. Further, we show that JMJD6 is correlated with the anti-cancer activity of indisulam, a "molecular glue" that degrades splicing factor RBM39, which complexes with JMJD6. The indisulam-mediated cancer cell killing is at least partly dependent on the glutamine-related metabolic pathway mediated by JMJD6. Our findings reveal a cancer-promoting metabolic program is coupled with alternative pre-mRNA splicing through JMJD6, providing a rationale to target JMJD6 as a therapeutic avenue for treating MYC-driven cancers.

67 **Introduction**

68 Metabolic reprogramming is a hallmark of cancer[1-3] which allows rapidly proliferating tumor cells to
69 acquire nutrients to meet their bioenergetic, biosynthetic, and redox demands[4]. One of the primary driving
70 forces in reprograming cancer cell metabolism is the deregulated MYC family proto-oncogenes (*C-MYC*,
71 *MYCN,* and *MYCL*)[5], which are known to encode master transcriptional factors that regulate metabolic
72 gene expression. MYC coordinates nutrient acquisition to produce ATP and key cellular building blocks
73 that increase cell mass and promote DNA replication and cell division[6]. The increase in total RNA and
74 protein synthesis by overactive MYC signaling leads to dysregulation of macromolecular processing
75 machineries including the spliceosome[7], and consequently pre-mRNA splicing[8-10], another hallmark of
76 MYC-driven cancers[7,9-12], for the purpose of cellular stress adaptation. *MYCN* amplification is one of the
77 most important biological features of high-risk neuroblastoma[13]. Transgenic mouse and zebrafish models
78 have demonstrated that MYCN is a neuroblastoma driver[14,15]. In tumors without *MYCN* amplification, *C-*
79 *MYC* is overexpressed, further indicating that neuroblastoma is a MYC-driven cancer. The metabolic
80 dependency of neuroblastoma has been widely studied by us and others[16-23]. A larger number of splicing
81 changes have also been noticed in high-stage neuroblastomas[24-26]. Splicing alterations lead to a
82 spliceosomal vulnerability that provides a new opportunity to develop transformative therapies by
83 disrupting aberrant pre-mRNA splicing[7,9-12]. We and others have shown that targeting the splicing factor
84 RBM39 by indisulam, a "molecular glue" that bridges RBM39 to E3 ubiquitin ligase DCAF15 for
85 proteasomal degradation, achieved an exceptional anti-tumor activity in neuroblastoma models[27,28].
86 Disruption of spliceosome by Pladienolide B also resulted in significant anti-tumor effect in
87 neuroblastoma models[26] However, how the dysregulated pre-mRNA splicing machinery and metabolism
88 are orchestrated in MYC-driven neuroblastoma has not been well elucidated. Whether metabolism
89 modulates the anti-cancer effect of splicing inhibition remains to be answered.

90 Next-generation sequencing studies have revealed only a few recurrent somatic mutations in
91 neuroblastoma at the time of diagnosis[29,30]. However, copy number alterations of chromosomal segments
92 such as 17q gain, 1p36 or 11q23 loss frequently occur in high-risk neuroblastoma. While attempts to
93 understand the functions of individual genes in these chromosomal segments have been reported (i.e.,
94 BIRC5[31], PHB[32], PPM1D[33], TRIM37[34] in 17q; ARID1A[35], CAMTA1[36], CASZ1[37], CHD5[38-40], KIF1Bβ[41-
95 43], miR-34a[44], RUNX3[45] in 1p36), the biological consequences of these genetic events in MYC-driven
96 tumors still remain largely unknown. Gain of 17q is the most frequent genetic event in high-risk
97 neuroblastoma and is associated with *MYCN* amplification[46]. In addition, in the transgenic *MYCN* mouse
98 model of neuroblastoma, the chromosomal locus syntenic to human 17q is partially amplified[47], indicating
99 that chromosome 17q is needed for MYC-mediated tumorigenesis.

100 JMJD6 is a JmjC domain–containing nuclear protein with iron- and 2-oxoglutarate–dependent
101 dioxygenase activity[48], whose coding gene is located on chromosome 17q25. While the histone arginine
102 demethylase activity of JMJD6 that catalyzes demethylation of H4R3me1/me2 is controversial[49], JMJD6
103 is a lysyl-5-hydroxylase that catalyzes 5-hydroxylation on specific lysine residues of target proteins[50].
104 JMJD6 has pleiotropic functions in normal physiology and in cancer[51-54]. We previously found that
105 JMJD6 is essential for the survival of neuroblastoma cells (including *MYCN*-amplified and *C-MYC*–
106 overexpressed cells)[55], which was further validated by an independent study[56], indicating that
107 neuroblastoma has JMJD6 dependency. However, the exact mechanism of JMJD6 in MYC-driven cancers
108 remains elusive. One study has shown that JMJD6 and BRD4 co-bind at antipause enhancers, regulating
109 promoter-proximal pause release of a large subset of transcription units[57]. By harnessing a similar
110 mechanism, JMJD6 promotes cell survival of glioblastoma *in vivo*[58]. These findings are particularly
111 interesting because BRD4 occupies exceptionally large super-enhancers associated with genes, including
112 *C-MYC* and *MYCN*[59-61], and the expression of those enhancers can be disrupted by BRD4 inhibitors, which
113 have a potent antitumor effect[59-62]. Here we show a new mechanism by which JMJD6 promotes
114 tumorigenesis mediated by the MYC oncogene in that JMJD6 interacts with a subset of RNA binding
115 proteins including RBM39 in neuroblastoma cells and regulates the alternative splicing of metabolic genes
116 that are involved in mitochondrial metabolism. "Glutamine addiction" is one key feature of MYC-driven
117 tumors. Glutaminase (GLS) is the enzyme responsible for conversion of glutamine to glutamate in the
118 process of glutaminolysis to feed the tricarboxylic acid (TCA) cycle and has two splice isoforms, GAC
119 (glutaminase C) and KGA (kidney-type glutaminase). We show that JMJD6 controls the alternative
120 splicing of KGA and GAC, and, consequently, impacts the central carbon metabolism in neuroblastoma.
121 Further we show that JMJD6 is correlated with the anti-cancer activity of indisulam, a "molecular glue"
122 that degrades the splicing factor RBM39. The indisulam-mediated cancer cell killing is at least partly
123 dependent on the glutamine-related metabolic pathway mediated by JMJD6. Our findings demonstrate a
124 new mechanism by which JMJD6 coordinates metabolic programs and alternative pre-mRNA splicing,
125 providing a rationale to target JMJD6 as a therapeutic target for MYC-driven cancers.
126

127 **Results**

128 **The essential genes for neuroblastoma cell survival on chromosome 17q target pre-mRNA splicing**
129 **and metabolism**

130 An incomplete understanding of the biological consequences of chromosome 17q gain remains a barrier
131 to the understanding of high-risk neuroblastoma. 1132 genes are located on 17q (**Supplementary table**
132 **1**). We surmised that some of the 17q genes are particularly important for neuroblastoma cell survival.

133 Analysis of the cancer dependency genes in neuroblastoma cell lines screened with the Avana sgRNA
134 library[63] revealed that 114 were essential to neuroblastoma (mean score <-0.4) (**Figure 1a**,
135 **Supplementary table 2**). Protein interaction network analysis followed by functional annotation revealed
136 that proteins encoded by these 114 essential genes formed distinct but interconnected modules including
137 RNA splicing (i.e., SRSF2, DDX5, DDX42, DHX8), mitochondrial metabolism (i.e., NDUFA8, COX11,
138 SLC25A10, SLC35B1), protein homeostasis (i.e., UBE2O, PSMB3, PSMC5), DNA repair (i.e., BRIP1,
139 BRCA1, RAD51C, RAD51D) and transcriptional regulation (i.e., PHF12, CBX1, SMARCE1, MED1),
140 as well as endocytosis (i.e., CHMP6, CTLC, EPN3, HGS, SNF8, VPS25) (**Figure 1b**). Using these 114
141 genes as a signature, we found that 81 of them were highly expressed in high-risk neuroblastomas, which
142 were enriched with MYCN amplification (**Figure 1c**). Correspondingly, neuroblastomas with high
143 expression levels of this gene signature were associated with a poorer event-free and overall survival of
144 patients (**Figure 1d, e**). These data demonstrate that 17q genes are involved in essential biological
145 processes and highly expressed in high-risk neuroblastomas.
146
147 **JMJD6 is required for neuroblastoma growth**
148 *JMJD6* was among these 114 essential genes. To understand the role of JMJD6, we examined the genetic
149 features of *JMJD6* in neuroblastoma and other types of cancers. Among the genes encoding JmjC-domain
150 containing proteins, *JMJD6* was the only one that was frequently amplified in neuroblastoma (**Figure 2a**).
151 High *JMJD6* expression was associated with poor event-free outcome, as shown by Kaplan-Meier analysis
152 (**Figure 2b**). To examine whether *JMJD6* amplification is limited to specific tumor types, we explored
153 genomic data from different cancers using the cBioportal program. *JMJD6* was amplified across multiple
154 types of adult cancers such as breast and liver cancer (**Supplementary Figure 1a**), and correlated with
155 worse relapse-free survival (**Supplementary Figure 1b**). We further compared the RNA-seq expression
156 of *JMJD6* in 2337 samples across over 20 pediatric cancer subtypes and found that *JMJD6* showed the
157 highest expression levels in neuroblastoma (**Supplementary Figure 1c**), suggesting that JMJD6 might be
158 particularly important in neuroblastoma. We validated this hypothesis using shRNA knockdown of
159 JMJD6 in *MYCN* amplified cells (BE2C, SIMA, KELLY, IMR32) and non-*MYCN* amplified cells (SK-
160 N-AS and CHLA20). The results showed that loss of JMJD6 greatly reduced the colony numbers in all
161 tested cell lines (**Figure 2c**), demonstrating that JMJD6 is essential to neuroblastoma cells regardless of
162 *MYCN* amplification. Neuroblastic tumors comprise a histologic spectrum that ranges from less-
163 differentiated neuroblastoma to well-differentiated ganglioneuroma. The extent of differentiation in the
164 tumor cells is correlated with prognostic significance[64]. We noticed that the loss of JMJD6 led to neurite
165 outgrowth (**Supplementary Figure 1d**), a unique structure of neuroblastoma cells differentiating *in vitro*.

166 This morphologic change suggests that JMJD6 is required to maintain cancer cell stemness. Lastly, we
167 validated that JMJD6 is essential to neuroblastoma growth in *MYCN* amplified (BE2C) and C-MYC
168 overexpressed (SK-N-AS) xenograft models (**Figure 2d, e**). Taken together, these data demonstrate that
169 loss of JMJD6 function impedes neuroblastoma cell survival and tumor growth.
170
171 **JMJD6 promotes MYC-mediated cellular transformation**
172 Next, we investigated whether gain of function of JMJD6 could facilitate MYC-mediated oncogenic
173 transformation. To test this, we used a NIH3T3 transformation assay that provides a straightforward
174 method to assess the transforming potential of an oncogene, which may lead to morphological
175 transformation and loss of contact inhibition, a typical feature of cellular transformation. Like the GFP
176 control (**Supplementary Figure 2a**), we found that NIH3T3 cells with overexpressed JMJD6 stopped
177 proliferation after being confluent (**Supplementary Figure 2b**), indicating JMJD6 alone is unable to
178 transform NIH3T3 cells. However, overexpression of MYCN induced foci formation with enhanced cell
179 death (**Supplementary Figure 2c**). Importantly, NIH3T3 cells with overexpressed MYCN and JMJD6
180 lost contact inhibition, accompanied with morphological change, and formed larger foci (**Supplementary**
181 **Figure 2d**), indicating that JMJD6 enhances MYCN activity to transform NIH3T3 cells. Interestingly,
182 MYCN alone also reprogramed metabolism of NIH3T3 cells as shown by the color change of the media,
183 indicative of acidic pH change, which was largely rescued by co-expression of JMJD6 (**Supplementary**
184 **Figure 2e**), suggesting that cells with enhanced lactate production by MYCN were directed to oxidative
185 phosphorylation by JMJD6. It is believed that the cell of origin of neuroblastoma is the progeny of neural
186 crest cells. We therefore tested the role of JMJD6 in MYC-mediated transformation using JoMa1, a cell
187 line derived from murine neural crest, by transducing GFP, JMJD6, MYCN and JMJD6/MYCN (**Figure**
188 **2f**). While JMJD6 showed no difference from GFP control in regulating cell proliferation, MYCN slightly
189 enhanced cell proliferation (**Figure 2g**). However, the combination of JMJD6 and MYCN remarkably
190 increased cell proliferation, mirrored by the colony formation assay which showed JMJD6/MYCN
191 induced rapid growth of colonies with distinct transformation morphology (**Figure 2g, h**). Implantation
192 of each group into immune-deficient mice led to tumor development of MYCN and JMJD6/MYCN groups
193 (**Figure 2i**). However, JMJD6/MYCN group tumors appeared to grow faster than the MYCN alone
194 tumors. Taken together, these data indicate that JMJD6 enhances the MYC-mediated transformation,
195 demonstrating the oncogenic role of JMJD6.
196
197 **JMJD6 regulates pathways engaged in pre-mRNA splicing and mitochondrial biogenesis in**
198 **neuroblastoma**

199 We surmised that loss of function of genes in the same functional module/pathway may induce similar
200 effects across different cell lineages, which in turn corroborates the hypothesis that JMJD6 is a player in
201 that signaling pathway. To test this hypothesis, we analyzed the dependency correlation of *JMJD6*
202 knockout and other genes (defined as co-dependency genes if they are positively correlated), by using the
203 DepMap data (https://depmap.org) that includes genome-wide knockout in 1027 cell lines of more than
204 20 cancer types (**Supplementary Table 3**), followed by pathway enrichment. The data showed that
205 JMJD6 co-dependency genes were significantly and positively correlated with spliceosome/mRNA
206 splicing (i.e., RBM39, SF3B1), ubiquitin-mediated proteolysis and endocytosis and a number of 17q25
207 genes, (**Figure 3a, c**), which mirrored the pathway network of 17q essential genes in neuroblastoma
208 (**Figure 1b**). JMJD6 knockout was negatively correlated with the knockout of genes housed at
209 chromosome 1p, which is frequently deleted in high-risk neuroblastoma, and oxidative phosphorylation
210 as well as protein translation (**Figure 3b, d**).
211
212 BRD4 is known to regulate MYC expression[61,65]. Previous studies have shown that JMJD6 and BRD4
213 interact to regulate gene transcription[56,58,66], suggesting that JMJD6 might directly modulate MYC
214 expression. To assess this possibility, we knocked down *JMJD6* in neuroblastoma cell lines BE2(C) and
215 SK-N-AS, which express *MYCN* and *C-MYC*, respectively, for RNA-seq analysis. The sequencing data
216 were analyzed for differential gene expression (**Supplementary Table 4**). Interestingly, loss of JMJD6
217 showed minimal impact on expression of *MYCN* in BE2C cells or *C-MYC* in SK-N-AS cells
218 (**Supplementary Figure 3a**), and western blot analysis did not show alteration of MYCN expression
219 although C-MYC protein was slightly downregulated by loss of JMJD6 (**Supplementary Figure 3b**).
220 However, BRD4 inhibitors drastically inhibited both MYCN and C-MYC expression in neuroblastoma
221 cells[59-61], suggesting that JMJD6 inhibition has a distinct effect from the BRD4 inhibition. Gene set
222 enrichment analysis for pathway engagement for the genes commonly downregulated or upregulated in
223 both cell lines revealed that loss of JMJD6 most significantly repressed the expression of genes involved
224 in pre-mRNA splicing, histones, and cell cycle G1/S checkpoint (**Figure 3e**), and enhanced the pathways
225 involved in mitochondrial functions and heat shock response (**Figure 3e**). Interestingly, the genes
226 transcribed from the mitochondrial genome were elevated in both cell lines (**Supplementary Figure 3c**),
227 suggesting that JMJD6 directly or indirectly regulates the transcription of mitochondrial genome. These
228 data are consistent with the co-dependency pathways of JMJD6 (**Figure 3a-d**). Depletion of JMJD6 in
229 both cell lines led to the downregulation of MYC signaling pathways (**Supplementary Figure 4**),
230 although ranked behind the pathways of splicing and metabolism, suggesting that the MYC pathways are

231 not primarily regulated by JMJD6. These data indicate that JMJD6 does not regulate the gene expression
232 of the MYC family of transcription factors but might indirectly regulate the MYC pathway.
233
234 To verify if JMJD6 regulates pre-mRNA splicing, we analyzed the RNA-seq using two algorithms. The
235 first one is event-based analysis to identify the altered exon splicing (**Figure 3f**). We found that
236 knockdown of JMJD6 dominantly affects the exon skipping (SE) although other splicing events were also
237 altered, albeit with a much smaller number (**Figure 3f**). Pathway analysis of common events in both BE2C
238 and SK-N-AS cells demonstrated that genes involved in metabolism and splicing are the most significantly
239 affected by loss of function of JMJD6 (**Figure 3g**). Using the second algorithm of RNA splicing analysis
240 previously developed (**Figure 3h**) that allows discovery of new isoforms of genes generated through
241 alternative splicing[67], we identified 580 genes in BE2C cells and 1018 genes in SK-N-AS cells undergoing
242 alternative splicing after JMJD6 knockdown, 133 of which were shared by both (**Figure 3h,**
243 **Supplementary Fig. 5, Supplementary Table 5**). The alternatively spliced genes were involved in a
244 variety of pathways (**Supplementary Table 6**). KEGG pathway enrichment analysis of the 133
245 commonly alternatively spliced genes showed that only metabolic pathway genes were significantly
246 enriched (**Figure 3f**), most of which are involved in mitochondrial bioenergetics and folate metabolism
247 (**Figure 3h**). Collectively, these data demonstrate that JMJD6 regulates RNA splicing of genes engaged
248 in mitochondrial metabolism, being one of the key mediators of the 17q locus activity in neuroblastoma.
249
250 **JMJD6 regulates alternative splicing of glutaminolysis gene GLS**
251 Overactive MYC signaling leads to altered macromolecular processing machineries in response to an
252 increase in total RNA and protein synthesis[7]. MYC is also a master regulator of cancer metabolism
253 involved in ribosomal and mitochondrial biogenesis, glucose and glutamine metabolism and lipid
254 synthesis, leading to the acquisition of bioenergetic substrates enabling the cancer cell to grow and
255 proliferate[68-70]. "Glutamine addiction" is one feature of MYC-driven cancer[71]. The pre-mRNA splicing
256 altered by JMJD6 knockdown included *GLS*, the key enzyme of glutaminolysis, prompting us to
257 investigate the *GLS* splicing mediated by JMJD6 knockdown. GLS is known to catalyze the conversion
258 of glutamine to glutamate, and is alternatively spliced to form two isoforms, GAC and KGA[72], with
259 different cellular localization and catalytic capacities[73]. The GAC isoform is more frequently upregulated
260 in cancer cells than KGA[74], and has been shown to be regulated by MYC[75-77], leading to a "glutamine
261 addiction" phenotype in MYC-driven tumors[71]. We found that loss of JMJD6 led to a splicing switch from
262 the GAC isoform (with exons 1-15) to the KGA isoform (with exons 1-14 and 16-19) (**Figure 4a**), which
263 was further confirmed by isoform-specific RT PCR (**Figure 4b**). We then investigated the expression of

264 GAC/KGA at the protein levels after JMJD6 knockdown. Western blot showed that the KGA isoform was
265 increased after JMJD6 knockdown in all three tested cell lines, SK-N-AS, BE2C and SIMA (**Figure 4c**).
266 Then we further validated the JMJD6 effect on GLS isoform expression by using a luciferase reporter that
267 indicates the isoforms of GAC and KGA. Indeed, JMJD6 knockdown significantly increased the
268 expression of the KGA reporter (**Figure 4d**). RNA-immunoprecipitation showed that JMJD6 bound to
269 *GLS* RNA (**Figure 4e**), suggesting that JMJD6 may directly regulate the splicing of *GLS*. We reasoned
270 that if the regulation of *GLS* splicing by JMJD6 was a bone fide mechanism, the expression levels of
271 *JMJD6* would correlate with the levels of *GAC/KGA* in tumors. Indeed, *JMJD6* was positively correlated
272 with *GAC* and negatively correlated with *KGA* in two independent neuroblastoma cohorts (**Figure 4f**),
273 supporting the hypothesis that JMJD6 is required to maintain the high ratio of *GAC*/*KGA* in cancer cells
274 by controlling their alternative splicing. Clinical relevance of *GAC* and *KGA* in neuroblastoma was
275 evidenced by the findings that high *GAC* was associated with a worse event-free survival and high *KGA*
276 was associated with a better event-free survival (**Figure 4g**), suggesting that the *GAC*/*KGA* ratio may play
277 a role in cancer progression. However, introduction of either GAC or KGA in BE2C cells or SKNAS cells
278 promoted colony formation (**Figure 4h, i**), indicating that enhanced glutaminolysis by either GAC or
279 KGA overexpression is pro-proliferative by gaining more ATPs.
280
281 **JMJD6 forms an interaction network with proteins involved in splicing and protein synthesis**
282 To understand the mechanism of JMJD6 in regulating splicing in neuroblastoma, we performed an
283 unbiased identification of JMJD6 interacting partners by introducing a flag-tagged JMJD6 into SK-N-AS
284 and BE2C cells, followed by immunoprecipitation to pull down the JMJD6 associated complex and
285 protein identification with mass spectrometry (**Figure 5a, Supplementary Table 7**). We found that
286 JMJD6 mainly interacted with two classes of proteins which are involved in RNA splicing and protein
287 synthesis in both cell lines, respectively (**Figure 5a, Supplementary Figure 6**). We then validated the
288 interactions of JMJD6 with splicing factors using immunoprecipitation and western blot, and
289 demonstrated JMJD6 formed a complex with these RNA binding proteins, including RBM39 (**Figure 5b**),
290 a therapeutic target of high-risk neuroblastoma[27]. Since JMJD6 also interacted with several molecules
291 involved in protein translation, we investigated if JMJD6 also regulates protein synthesis by using an
292 approach, Click-IT AHA to label the newly synthesized proteins, followed by western blot assessment
293 (**Figure 5c**). Interestingly, overexpression of JMJD6 greatly reduced total protein synthesis (**Figure 5c**),
294 suggesting that JMJD6 may antagonize protein production.
295

296 Then we determined if the splicing factors interacting with JMJD6 also regulate GLS isoform expression.
297 Among the splicing factors with which JMJD6 interacted, CPSF6 has been previously shown to regulate
298 the alternative splicing of *GLS*[78]. We validated the function of CPSF6 in neuroblastoma cells and found
299 that, indeed, loss of CPSF6 led to a dramatic switch from GAC to KGA in BE2C and SK-N-AS cells
300 (**Figure 5d, 5e**). Previous studies showed that JMJD6 and U2AF2 (U2AF65) interact to regulate
301 splicing[50,79]. We also found that knockdown of U2AF2 resulted in a similar phenotype to JMJD6
302 knockdown in that the expression of KGA isoform was greatly increased in both cell lines (**Figure 5d,**
303 **5e**). These data collectively support the functions of JMJD6 in regulating the splicing of metabolic genes
304 and protein homeostasis in MYC-driven neuroblastoma.
305
306 **JMJD6 regulates production of TCA intermediates and nucleoside triphosphate**
307 To further dissect the biological consequences of loss of function of JMJD6, we created stable JMJD6
308 knockout clones (**Supplementary Figure 7**) and defined the metabolite spectrum affected by loss of
309 function by using liquid chromatography with tandem mass spectrometry (LC-MS/MS). JMJD6 knockout
310 greatly reduced the production of tricarboxylic acid cycle (TCA) intermediates (i.e., oxoglutarate,
311 fumarate) and nucleoside triphosphate (ATP, CTP, GTP) (**Figure 6a**), indicating that JMJD6 is a key
312 bioenergetics regulator in cancer cells. Pathway analysis revealed that the reduced metabolites were
313 involved in the Warburg effect, TCA, pentose phosphate pathway, and mitochondrial electron transport
314 chain (**Figure 6b**), all of which are critical for providing cancer cell bioenergetics for proliferation and
315 survival. Oxoglutarate (α-ketoglutarate) and fumarate are downstream products of glutaminolysis (**Figure**
316 **6c**). We reasoned that cellular metabolites such as glutamate and oxoglutarate may predict the cytotoxic
317 effect of loss-of-function of JMJD6. If cells have higher levels of glutamate and oxoglutarate, they might
318 be less dependent on JMJD6 due to their higher capacity of buffering against reduced glutaminolysis. To
319 test this hypothesis, we used DepMap data that included 225 metabolites in 928 cancer cell lines from
320 over 20 lineages[80], and analyzed the correlation of each metabolite with *JMJD6* gene dependency. The
321 data showed that cells with high levels of AMP, glutamate, alanine, 2-hydroxyglutarate and 2-oxoglutarate
322 were more resistant to JMJD6 knockout, while cells with high levels of lactose and sucrose were more
323 sensitive to JMJD6 knockout (**Figure 6d, Supplementary Table 8**). High levels of AMP activate AMP
324 kinase (AMPK), consequently leading to enhanced fatty acid oxidation to stimulate ATP production while
325 alanine can be converted to pyruvate to provide acetyl-CoA to fuel the TCA cycle (**Figure 6c**). Therefore,
326 high levels of AMP and alanine may provide cells alternative bioenergetics sources for survival. These
327 data further indicate that JMDJ6 function is wired into the regulation of mitochondrial metabolism.
328

329 **JMJD6 determines the efficacy of indisulam, a molecular glue degrading splicing factor RBM39**
330 Dysregulated splicing as a vulnerability of MYC-driven cancers provides a rationale to target
331 neuroblastoma by using splicing inhibitors as a therapeutic approach. We and others have recently
332 reported that indisulam, a "molecular glue" that selectively degrades the splicing factor RBM39, is
333 exceptionally effective at causing tumor regression in multiple high-risk neuroblastoma models without
334 overt toxicity[27,28], suggesting indisulam has translational potential. Understanding the factors determining
335 the efficacy of indisulam or any other drug is critical for developing precision therapy, combination
336 therapy or preventing therapy resistance. In addition to complexing together (**Figure 5a, b**), JMJD6 and
337 RBM39 exhibit significant correlation of co-dependency in cancer cells, namely, cancer cells have similar
338 dependency on JMJD6 and RBM39 for survival (**Supplementary Table 3, Figure 7a**). These data
339 indicate that JMJD6 may play a role in modulating the effect of indisulam. To test this hypothesis, we
340 performed GSEA to identify the differential pathways between indisulam-sensitive and indisulam-less
341 sensitive neuroblastoma cells. It turned out that histone lysine demethylase (HDM) genes including
342 JMJD6 are the in the only gene signature that is significantly enriched in indisulam-sensitive cells (**Figure**
343 **7b, c, d**). Indeed, knockout of JMJD6 led to partial but significant resistance to indisulam treatment of
344 SK-N-AS cells (**Figure 7e-g**) and BE2C cells (**Figure 7h-j**), supporting that cells with high JMJD6
345 expression are more dependent on RBM39. Since we found that JMJD6 plays a key role in modulating
346 glutaminolysis, we tested if expression of GAC or KGA could affect the activity of indisulam.
347 Interestingly, overexpression of either GAC and KGA renders BE2C and SK-N-AS cells more resistant
348 to indisulam treatment (**Figure 7k-n**), suggesting that enhanced glutaminolysis may confer therapeutic
349 resistance to spliceosome inhibition.
350
351 **Discussion**
352 MYC is an oncogenic driver of many types of cancer and plays a pivotal role in regulating glycolysis,
353 glutaminolysis, nucleotide and lipid synthesis, and ribosome and mitochondrial biogenesis[6]. Recent
354 studies have revealed that there is also an interplay between MYC and pre-mRNA splicing machinery[7-
355 10,81-84]. Pre-mRNA splicing is an essential biological process catalyzed by the spliceosome to produce
356 mature mRNAs[85,86]. Over 90% of multiexon genes in the human genome undergo alternative splicing[87,88],
357 which significantly expands the diversity of the proteome and consequently impacts various biological
358 functions[89,90]. In this study, we found that the chromosome 17q locus, which is frequently gained in MYC-
359 driven cancers, houses numerous genes essential to cancer cell survival that are implicated in pre-mRNA
360 splicing, ribosome and mitochondrial biogenesis and other biological functions. Particularly, JMJD6,
361 which is located on 17q25 and is amplified in a number of cancer types, physically interacts with a subset

362 of splicing factors such as RBM39 and regulates the alternative splicing of metabolic genes. Depletion of
363 JMJD6 inhibits cancer cell proliferation and impedes tumor growth while overexpression of JMJD6
364 promotes MYC-mediated tumorigenesis, suggesting that JMJD6 and potentially other 17q genes have
365 oncogenic functions in cellular transformation. Previous studies suggest that JMJD6 and BRD4 interact
366 to regulate gene transcription[56,66]. However, our unbiased identification of the JMJD6 interactome only
367 identified a subset of proteins involved in mRNA splicing and protein translation in neuroblastoma cells,
368 suggesting that JMD6 may predominantly regulate protein homeostasis to facilitate MYC-mediated
369 transformation. Nevertheless, we cannot exclude the possibility that our immunoprecipitation conditions
370 were too harsh, leading to dissociation of proteins that loosely or dynamically bind to JMJD6.
371
372 MYC-induced metabolic reprogramming triggers cellular dependency on exogenous glutamine as a source
373 of carbon for mitochondrial membrane potential maintenance and macromolecular synthesis[2], leading to
374 "glutamine addiction"[2]. Glutaminolysis is a process by which GLS and GLS2 convert glutamine to
375 glutamate, which is, in turn, converted by glutamate dehydrogenase or transaminase to 2-oxoglutarate that
376 is further catabolized in the TCA cycle. Additionally, glutamate is a substrate for production of
377 glutathione, an important antioxidant. We previously showed that neuroblastoma relies on MYCN-
378 induced glutaminolysis for survival[20]. In this study, our RNA-seq barely detected the expression of *GLS2*
379 in the neuroblastoma cell models we used, indicating that GLS is the major enzyme that catalyzes
380 glutamine in these model systems. *GLS* has two isoforms, *GAC* and *KGA*, resulting from alternative
381 splicing. KGA is mainly localized in the cytoplasm while GAC is localized in mitochondria and has a
382 higher basal activity[73]. *GAC* mRNA levels strongly correlate with the conversion of glutamine to
383 glutamate, as a proxy for GAC activity[91]. The positive correlation of *JMJD6* and *GAC* suggests that the
384 JMJD6-high tumors have enhanced glutaminolysis activity. CSPF6 and the noncoding RNA *CCAT2* have
385 been reported to regulate the splicing of GLS isoforms[78,92]. Interestingly, we found that depletion of
386 JMJD6 leads to a *GLS* isoform switch from *GAC* to *KGA*, indicating that JMJD6 is involved in alternative
387 splicing of *GLS*. We further found that JMJD6 physically interacts with CPSF6 in a splicing network and
388 validated that loss of CPSF6 results in remarkable induction of the KGA isoform. We further validated
389 that other splicing factors such as U2AF2 also interact with JMJD6 to regulate the GLS isoform switch.
390 These data indicate that cancer cells can adjust metabolism through alternative splicing to produce
391 enzymes with distinct subcellular localization and activity that promote cellular transformation or
392 progression of an oncogenic phenotype. The cooperation of JMJD6 and MYC in cellular transformation
393 further supports the hypothesis that JMJD6 is needed for metabolic reprogramming triggered by MYC.
394 However, overexpression of either GAC or KGA promotes cell proliferation, suggesting that the switching

395 of KGA/GAC is a cellular fitness mechanism in response to interruption of the spliceosome by adjusting
396 the metabolic rate. Within the tumor microenvironment (i.e., replete and deplete oxygen and nutrient
397 supply) GLS activity is possibly finely tuned through splicing mechanism for adaption.
398
399 Additionally, we found that JMJD6 physically interacts with a subset of ribosomal proteins that are
400 responsible for protein translation. Interestingly, overexpression of JMJD6 reduces global protein
401 synthesis. A recent study showed that MYC overactivation leads to proteotoxic stress in cells by enhancing
402 global protein synthesis, consequently causing cell death[93]. The increased global protein synthesis by
403 MYC needs to be buffered through loss of DDX3X, a regulator of ribosome biogenesis and global protein
404 synthesis, for lymphomagenesis[93]. Our findings suggest that, besides the functions in regulating alternative
405 splicing for metabolism, JMJD6 is involved in MYC-mediated cell transformation by buffering unwanted
406 proteotoxic stress due to high rate of protein synthesis induced by MYC (**Figure 8**).
407
408 Neuroblastoma is responsible for as much as 15% of childhood cancer mortality[94]. With current intensive
409 multimodal therapies, 5-year survival rates for high-risk patients remain less than 50%[95-98]. In addition,
410 survivors of high-risk disease have a significant risk of developing long-term side effects including
411 subsequent malignant neoplasms due to cytotoxic chemotherapy and radiotherapy[99,100]. Unfortunately,
412 developing effective precision therapies against high-risk neuroblastoma has been challenging due to the
413 lack of targetable recurrent mutations in neuroblastoma[29,30,101]. Our previous study showed that indisulam,
414 the splicing inhibitor that targets RBM39, a JMJD6-interacting partner, induced a durable complete
415 response in multiple high-risk neuroblastoma models, supporting its potential use in future clinical trials.
416 Our current study showed that JMJD6 expression is positively correlated with the effect of indisulam, and
417 knockout of JMJD6 confers resistance to indisulam treatment. In line with the biological functions of
418 JMDJ6 in regulating GLS isoform expression and mitochondrial metabolism, overexpression of GAC or
419 KGA also caused resistance to indisulam treatment. These data indicate that JMJD6 could serve as a
420 biomarker that predicts response to indisulam or other splicing inhibitors.
421
422 **Materials and Methods**
423
424 **Cell lines.** KELLY, SIMA, BE2C, IMR32, SK-N-AS, CHLA20 were cultured in 1X RPMI1640 (Corning,
425 15-040-CV) supplemented with 10% Fetal Bovine Serum (Sigma-Aldrich, F2442), 1% L-Glutamine
426 (Corning, A2916801). NIH3T3 and 293T cells were cultured in 1X DMEM supplemented with 10% Fetal
427 Bovine Serum (Sigma-Aldrich, F2442), 1% L-Glutamine (Corning, A2916801). All cells were maintained

428 at 37 °C in an atmosphere of 5% CO_2. JoMa1 cells were kindly provided by Dr. Schulte (Department of
429 Pediatric Oncology and Hematology, University Children's Hospital Essen, Essen, Germany) were
430 cultured in NCC Medium: DMEM (4.5 mg/ml Glucose, L-Glutamine, Pyruvate): Ham's F12 (1:1) was
431 supplemented with: 1% N2-Supplement (Invitrogen, no. 17502-048), 2% B27-Supplement (Invitrogen,
432 no. 17504-044), 10ng/ml EGF (Invitrogen), 1ng/ml FGF (Invitrogen), 100U/ml Penicillin–Streptomycin
433 (Invitrogen) and 10% Chick-Embryo-Extract (Gemini Bio-Products, CA). Neural crest culture medium
434 was supplemented with 200 nM 4-OH-tamoxifen (Sigma no. H7904) in routine culture to ensure nuclear
435 localization of c-MycERT and JoMa1 cell proliferation. JoMa1 cells were grown on cell culture flask/dish
436 coated with fibronectin, NCC-medium supplemented with 200nm 4-OHT was changed daily. Cells were
437 passaged after 3–4 days in culture when 70% confluence was reached (4 X 10^6 cells/10 cm dish).
438 All human-derived cell lines were validated by short tandem repeat (STR) profiling using PowerPlex®
439 16 HS System (Promega) once a month. Additionally, a polymerase chain reaction (PCR)-based method
440 was used to screen for mycoplasma once a month employing the LookOut® Mycoplasma PCR Detection
441 Kit (MP0035, Sigma-Aldrich) and JumpStart™ Taq DNA Polymerase (D9307, Sigma-Aldrich) to ensure
442 cells were free of mycoplasma contamination.
443
444 **Antibodies.** GAPDH (Cell Signaling Technology, 5174s, Rabbit antibody), MYCN (Santa Cruz
445 Biotechnology, 53993, Mouse antibody) , FLAG (Sigma, F1804, Mouse antibody), Biotin (Bethyl
446 Laboratories, A150-109A Rabbit), ACTIN (Sigma, A3854, mouse antibody), PUF60 (Thermo
447 Fisher, PA5-21411, Rabbit antibody), U2AF2 (Novus Biologicals, NBP2-04140, Rabbit antibody),
448 CPSF6 (Bethyl Laboratories, 357A,Rabbit antibody), DHX40 (Novus Biologicals, NBP1-91834,
449 Rabbit antibody), DHX8 (Abcam, AB181074, Rabbit antibody), LUC7L1 (Novus Biologicals,
450 NBP2-56401, Rabbit antibody), LUC7L2 (Novus Biologicals, NBP2-33621, Rabbit antibody), LUC7L3
451 (Novus Biologicals, NBP1-88053, Rabbit antibody), RBM39 (ATLAS, HPA001519, Rabbit antibody),
452 GLS (KGA-specific), (Proteintech,20170-1-AP, Rabbit antibody), GLS(GAC-Specific) (Proteintech,
453 19958-1-AP, Rabbit antibody), JMJD6 (ATLAS, HAP059156, Rabbit antibody), JMJD6 (Santa Cruz
454 biotechnology, sc-28348, Mouse antibody).
455
456 **Retroviral plasmids and retrovirus packaging.** MSCV-IRES-GFP and MSCV-IRES-mCherry were
457 obtained from St Jude Vector Core. Human JMJD6 and murine MYCN were subcloned into MSCV-IRES-
458 GFP and MSCV-IRES-mCherry, respectively. The MSCV-CMV-CMV-Flag-HA-JMJD6 was purchased
459 from Addgene (Addgene # plasmid 31358). The retrovirus packaging was done as described in the
460 following procedure. Briefly, HEK93T cells were transfected with viral vectors by combining 5μg of

461 target vector, 4.4μg of pMD-old-gag-pol, and 0.6μg of VSV-G plasmids in 400uL of DMEM without
462 serum or L-glutamine. PEIpro transfection reagent (Polyplus 115-010) was added at 2:1 (PEIpro μL: μg
463 of plasmid) per 100mm dish of cells and mixed well, and incubated at RT for at least 20 minutes, prior to
464 adding cells. The following day, fresh medium was added to cells. For 3-4 days, viral media was
465 harvested and replaced twice per day. Viral media was centrifuged at 1500RPM for 10 minutes and
466 filtered through a 0.45um vacuum filter. Virus was concentrated by ultracentrifugation at 28.5kRPM for
467 2 hours at 4C, aspirated, and resuspended in either OptiMEM or PBS, aliquoted, and frozen at -80C until
468 use. Wasie, add information for GAC/KGA here.
469
470 **siRNA transfection**. 25uM of each siRNA oligo was resuspended in 500uL of prewarmed Opti-MEM,
471 reduced serum medium (Gibco Life technologies #31985-070) in 6 well plates. To each well, 7μL of
472 RNAiMax (Invitrogen Lipofectamine RNAiMAX transfection reagent 13778100) was added, mixed, and
473 left at room temperature for 10 minutes. After incubation, 100,000 cells of each indicated cell line were
474 added to each well in a total of 2mL volume with RPMI medium supplemented with 10% FBS. JMJD6
475 siRNA#43, 5-CCAAAGUUAUCAAGGAAA-3; JMJD6 siRNA#45, 5-
476 CAGUGAAGAUGAAGAUGAA-3. U2AF2 siRNA#1 AGAAGAAGAAGGUCCGU; U2AF2 siRNA#2
477 GUGGCAGUUUCAUAUUUG. CPSF6 siRNA#1 GGAUCACCUUCCAAGACA. CPSF6 siRNA#2
478 AGAACCGUCAUGACGAUU.
479
480 **SDS-PAGE and Western blot.** Cells were washed twice with ice-cold phosphate-buffered saline (PBS)
481 and directly lysed on ice with 2X sample loading buffer (0.1 M Tris HCl [pH 6.8], 200 mM dithiothreitol
482 [DTT], 0.01% bromophenol blue, 4% sodium dodecyl sulfate [SDS] and 20% glycerol). On ice, cell
483 lysates were sonicated once with a 5 second bursts at 40% amplitude output (Sonics, VIBRA CELL)
484 followed by 25 minutes heating at 95 °C. After the cell lysates were centrifuged at 13,000 × g at room
485 temperature for 2 mins, 10-20 μl of the cell lysates were separated on 4-15% Mini-PROTEAN® TGX™
486 Stain-Free™ Protein Gels from Bio-Rad and transferred to methanol-soaked polyvinylidene difluoride
487 (PVDF) membranes (Millipore). Lysates for RBM39 G268V mutant cell lines and DCAF15 genetically
488 modified cells were generated as previously described[102]. Membranes were blocked in PBS buffer
489 supplemented with 0.1% TWEEN 20 and 5% skim milk (PBS-T) and incubated for 1 hour at room
490 temperature under gentle horizontal shaking. Membranes were incubated overnight at 4 °C with the
491 primary antibodies. The next day, membranes were washed 3 times (for 5 minutes) with PBS-T at room
492 temperature. Protected from light, membranes were then incubated with goat anti-mouse or goat anti-
493 rabbit HRP-conjugated secondary antibodies (1:5,000) for 1 hour at room temperature, followed by three

494 5-minite washes with PBS-T at room temperature. Lastly, membranes were incubated for 1 minute at
495 room temperature with SuperSignal West Pico PLUS Chemiluminescent Substrate (34580, Thermo Fisher
496 Scientific) and the bound antigen-antibody complexes were visualized using Odyssey Fc Imaging System
497 (LI-COR Corp., Lincoln, NE).
498
499 **RNA extraction and RT-PCR isoforms of GLS.** RNA was extracted using RNeasy® Plus Mini Kit
500 (Qiagen, reference # 74136) following the manufacturer's protocol. cDNA was prepared in 20ul reaction
501 from 500ng of total RNA using Superscript™ IV First Strand Synthesis System (Invitrogen, reference #
502 1809105) kit. Real-time PCR reactions were run in triplicates (n=3) in the 7500 Real-time PCR system by
503 Applied Biosystems (Thermo Fisher Scientific) using power SYBR Green PCR master mix (Applied
504 Biosystems, reference # 4367660). ΔΔCT methods were applied to analyze the results. The following
505 primers were used to perform the quantitative Real-time PCR- GAPDH (Forward:
506 AACGGGAAGCTTGTCATCAATGGAAA, Reverse: GCATCAGCAGAGGGGGCAGAG), GAC
507 (Forward: GAGGTGCTGGCCAAAAAGCCT, Reverse: AGGCATTCGGTTGCCCAAACT), KGA
508 (Forward: CTGCAGAGGGTCATGTTGAA, Reverse: ATCCATGGGAGTGTTATTCCA).
509
510 **Lentiviral packaging of pLenti and shRNA.** The GAC and KGA cDNAs were synthesized by Genscript
511 company and cloned into pLenti vector. The TRC lentiviral-based shRNA knockdown plasmids for
512 JMJD6 were purchased from Horizon Discovery (sh#46: RHS3979-201781036,
513 TTAAACCAGGTAATAGCTTCG; sh#47: RHS3979-201781037, ATCTTCACTGAGTAGCCATCG)
514 The lentiviral shJMJD6 and shControl (pLKO.1) particles were packaged by Vector Lab at St Jude.
515 Briefly, HEK293T cells were transfected with shRNA constructs and helper plasmids (pCAG-kGP1-1R,
516 pCAG4-RTR2, and pHDM-G). The 48- and 72-hr post-transfection replication-incompetent lentiviral
517 particles were harvested and transduced into cells with 8μg/ml of polybrene. 48 hours later, 1 μg/ml of
518 puromycin was added for selection for additional 48 hours before injection into mice or immunoblotting.
519
520 **JMJD6 CRISPR KO method**. Genetically modified neuroblastoma cells were generated by using
521 CRISPR-Cas9 technology. Briefly, 400,000 NB cells were transiently co-transfected with 100pmol of
522 chemically modified gRNA (GGACTCTGGAGCGCCTAAAA) (Synthego), 33pmol of Cas9 protein (St.
523 Jude Protein Production Core), 200ng of pMaxGFP (Lonza), and, using solution P3 and program DS-150
524 in small cuvettes according to the manufacturer's recommended protocol. Five days post-nucleofection,
525 cells were sorted for GFP+ (transfected) cells and plated as single cells into 96-well plates. Cells were

526 clonally expanded and screened for the desired modification using targeted next generation sequencing
527 followed by analysis with CRIS.py (https://pubmed.ncbi.nlm.nih.gov/30862905/).
528
529 **Colony formation for JoMa1 cells**. Matrigel was kept at 4ºC to being liquified for 6 hours. 50µL of
530 Matrigel per 1 square centimeter area was added to 24-well plate without air bubble. The 24-well plate
531 was kept at 37ºC in cell culture incubator till it was solidified. 200 of JoMa1 cells transduced with GFP,
532 JMJD6, MYCN, MYCN+JMJD6 in DMEM:F12 enriched media without tamoxifen were seeded onto the
533 24-well coated with Matrigel. This was done in triplicate. Cells were checked daily, and media were
534 changed every 3 days without disturbing the Matrigel by removing and adding media gently. To stain the
535 colonies, cells were fixed by formaldehyde (3.7% in PBS) for 2 min at room temperature, followed by
536 permeabilization with 100% methanol (not ice-cold) for 20min at room temperature. The colonies were
537 stained by 0.4% crystal violet.
538
539 **Crystal Violet Staining.** After removing media, cells were washed with Dulbecco's phosphate buffered
540 saline without calcium or magnesium (DPBS, Lonza) and treated with 4% formaldehyde in PBS (PFA)
541 for 20 minutes. Once PFA was removed, cells were stained with 0.1% crystal violet stain for 1 hour.
542 KGA/GAC overexpression colony formation: 5000 cells were plated of BE2C control, KGA and GAC
543 overexpressing cells and were culture for 7 days; 10,000 cells were plated of SKNAS control, KGA and
544 GAC overexpressing cells and were culture for 7 days (n=3). After 7 days, medium was removed and
545 cells were washed with Dulbecco's PBS (DPBS) (DPBS, Lonza) and treated with 4% formaldehyde in
546 PBS [paraformaldehyde (PFA)] for 30 min. PFA was later removed and cells were stained with 0.1%
547 crystal violet stain for 1 hour. Experiments were repeated twice. Indisulam treatment on WT and JMJD6-
548 KO cell lines: JMJD6-WT and KO cells were plated in 12-well plate (50,000 cells/well for SKNAS) and
549 6-well plate (5,000 cells/well for BE2C) (n=3). Next day, cells were treated with Indisulam with indicated
550 concentration for 7 days (SKNAS cells) and 5 days (BE2C cells). Crystal violet staining was performed
551 to visualize and quantify the colony formation. Experiments were repeated twice. Indisulam treatment on
552 KGA/GAC overexpressing cell lines: 10,000 BE2C and 100,000 SKNAS control, KGA and GAC
553 overexpressing cells were plated in 6-well plate (n=3). Next day, cells were treated with Indisulam for 7
554 days. Crystal violet staining was performed to visualize and quantify the colony formation. Experiments
555 were repeated twice.
556
557 **Click-iT AHA labeling assay for metabolic labeling of newly synthesized proteins**. Click-iT was
558 performed as previously described. Briefly, cells were plated at 5 million cells per 100mm dish in RPMI

559 supplemented with 10% FBS. Cells were washed with warm PBS and replaced with methionine-free
560 medium (Thermo 21013024 supplement with glutamine and sodium pyruvate) for 1 hour at 37° C in 5%
561 CO_2. Following, fresh methionine-free media containing 50µM of Click-iT AHA (L-azidohomoalanine)
562 (Thermo C10102) was added to the cells for 2 hours at 37°C. After AHA-labeling, cells were washed with
563 warm PBS and lysed with 1% SDS, 50mM Tris-HCl, (pH 8.0) supplemented with phosphatase inhibitors
564 (PhosSTOP, Sigma) and protease inhibitors (cOmplete mini, Roche) by applying the buffer directly to the
565 plate, incubating the cells on ice for 30 minutes, tilting the plates, and collecting the lysate. Lysates were
566 briefly sonicated, vortexed for 5 minutes, and centrifuged at 18,000xg for 5 minutes at 4°C. Total protein
567 quantification was assayed using the EZQ Protein Quantification Kit (Thermo R33200) according to the
568 manufacturer's protocol and results were read on a fluorescence-based microplate reader (BioTek Synergy
569 2). Click chemistry of the biotin-alkyne (PEG4 carboxamide-propargyl biotin) (Thermo B10185) to the
570 AHA-labeled lysates was performed using the Click-iT Protein Reaction Buffer Kit (Thermo C10276)
571 using a concentration of 40µM biotin-alkyne per click reaction (and no biotin-alkyne added for controls).
572 Following the click reaction, samples were either assayed for total biotinylated protein by following the
573 manufacturer's protocol. For total biotinylated protein, briefly, 600µL of methanol, 150µL of chloroform,
574 and 400µL of megaOhm water was sequentially added and vortexed, followed by centrifugation at
575 18,000xg for 5 minutes. The upper aqueous phase was discarded, and 450µL of methanol was added,
576 vortexed, and centrifuged again at 18,000xg for 5 minutes. This methanol step was performed in duplicate
577 to remove residual reaction components. Protein pellets were allowed to air dry and resuspended in a
578 suitable volume of sample buffer and heated prior to western blot analysis.
579
580 **Immunoprecipitation.** $5X10^6$ BE2C and SK-N-AS cells expressing Flag-JMJD6 were cultured in 150cm
581 dish with complete RPMI media. Cells were washed twice with cold PBS after reaching 95% confluency,
582 then lysed in 1ml lysis buffer (50mM Tris-HCl, pH 7.4, 150mM NaCl, 1mM EDTA, 1% Trion-X100 with
583 complete protease inhibitors (Sigma 11836170001, added fresh) and PhosSTOP (Sigma 4906845001).
584 Cells were scrapped into a 1.5mL Eppendorf tube and incubated on ice for 15min, which were mixed by
585 vortex every 5 min. Cell lysates were spun by 135000rpm for 10min at 4C. The supernatant was
586 transferred to a new tube. The cell lysates were subject to immunoprecipitation using M2 anti-Flag beads
587 (Sigma, M8823) overnight by rocking at 4°C. The following day, beads were washed 3X with buffer and
588 eluted with 5 packed gel volumes of FLAG peptide in TBS buffer (3uL of stock FLAG peptide at 5ug/uL
589 per 100uL of TBS buffer) while rotating at 4°C for 30 minutes. Beads were briefly spun and the
590 supernatant was removed from the beads (eluate). This elution step was repeated one more time and
591 pooled with the first eluate. Prior to western blot, input, flow throughs, and elution samples were

592 processed by adding 4X sample buffer supplemented with 50mM DTT and heated at 75ºC for 10 minutes
593 prior to running on a gel.
594
595 **RNA-immunoprecipitation.** SK-N-AS cells expressing Flag-JMJD6 were grown in a 10-cm dish in
596 RPMI complete media. After 70% confluency, cells were washed with cold PBS twice and then were
597 subject to lysis with Polysome Lysis Buffer (100mM KCl, 5mM $MgCl_2$, 10mM HEPES, pH7.0, 0.5% NP-
598 40, 1mM DTT, 100 U/ml RAasin RNase inhibitor (Promega, N2511), 2mM vanadyl ribonucleoside
599 complexes solution (Sigma, 94742), 25µL protease inhibitor cocktail for mammalian cells (Sigma,
600 P8340)). Cell lysates were precleared with magnetic IgG beads for 1 hour. The cell lysates were subject
601 to immunoprecipitation using M2 anti-Flag beads (Sigma, M8823) overnight by rocking at 4ºC. The same
602 amounts of lysates were saved at -80ºC for input RNA extraction. The beads were washed with 250 µL
603 Polysome Lysis Buffer for 4 times, flowed by washing with Polysome Lysis Buffer containing 1M urea.
604 RNA was released by adding 150µL of Polysome Lysis Buffer containing 0.1% SDS and 45µg protease
605 K (Ambion, AM2548) and incubated at 50ºC for 30min. RNA was extracted with phenol-chloroform-
606 isoamyl alcohol mixture (Sigma, 77618). RNA was recovered by adding 2µL of GlycoBlue (15mg/ml,
607 Ambion, AM9516), 36µL of 3M sodium acetate and 750µL ethanol followed by incubation at -20ºC for
608 overnight. RNA was precipitated with 70% ethanol and air dried, followed by resuspension with RNase-
609 free water followed by DNaseI (Promega, M6101) treatment to remove genomic DNA. The resultant
610 RNAs were subjected to RT-qPCR analysis using 3 sets of GAC and KGA primers and 18S rRNA as
611 control. 18S rRNA F: GCTTAATTTGACTCAACACGGGA; 18S rRNA R:
612 AGCTATCAATCTGTCAATCCTGTC. GLS-GACiso_F: GAGGTGCTGGCCAAAAAGCCT; GLS-
613 GACiso_R: AGGCATTCGGTTGCCCAAACT. GLS-KGAiso_F: CTGCAGAGGGTCATGTTGAA;
614 GLS-KGAiso_R: ATCCATGGGAGTGTTATTCCA. KGA_set2_F:
615 GCAGCCTCCAGGTGCTTTCA; KGA_set2_R: GTAATGGGAGGGCAGTGGCA. KGA_set3_F:
616 TGCCCGACACTGCCCTTTAG; KGA_set3_R: CCTGCCAGACAGACAACAGCA. GAC_set2_F:
617 TGCTTCTCAAGGCCTTACTGC; GAC_set2_R: AGGCATTCGGTTGCCCAAACT. GAC_set3_F:
618 CCTTCTAGAGGTGCTGGCCAAA; GAC_set3_R: TGCAACACAAATATGCAGTAAGGC. For
619 validation of protein immunoprecipitation, 20% of beads after overnight incubation were removed and
620 processed as follows: Beads were washed 3X with buffer and eluted with 5 packed gel volumes of FLAG
621 peptide in TBS buffer (3µL of stock FLAG peptide at 5µg/µL per 100uL of TBS buffer) while rotating at
622 4ºC for 30 minutes. Beads were briefly spun and the supernatant was removed from the beads (eluate).
623 This elution step was repeated one more time and pooled with the first eluate.
624

625 **Identification of JMJD6 interacting partners by LC-MS/MS**. Protein samples were run on a short gel
626 as described in a previously published protocol[103]. Proteins in the gel bands were reduced with
627 dithiothreitol (DTT) (Sigma) and alkylated by iodoacetamide (IAA) (Sigma). The gel bands were then
628 washed, dried, and rehydrated with a buffer containing trypsin (Promega). Samples were digested
629 overnight, acidified and the resulting peptides were extracted. The extracts were dried and reconstituted
630 in 5% formic acid. The peptide samples were loaded on a nanoscale capillary reverse phase C18 column
631 by a HPLC system (Thermo EASY-nLC 1000) and eluted by a gradient. The eluted peptides were ionized
632 and detected by a mass spectrometer (Thermo LTQ Orbitrap Elite). The MS and MS/MS spectra were
633 collected over a 90-min liquid chromatography gradient. Database searches were performed using Sequest
634 (version 28 revision 13) search engine against a composite target / decoy Uniprot human protein database.
635 All matched MS/MS spectra were filtered by mass accuracy and matching scores to reduce protein false
636 discovery rate to <1%. Spectral counts, matching to individual proteins reflect their relative abundance in
637 one sample after the protein size is normalized. The spectral counts between samples for a given protein
638 was used to calculate the p-value based on G-test [104].
639
640 **Metabolome profiling by LC-MS/MS**. JMJD6 knockout or parental SK-N-AS cells were cultured in 6-
641 well plates to ~85% confluence and washed with 2 mL ice cold 1X Phosphate-Buffered Saline (PBS). The
642 cells were then harvested in 300 µL freezing 80% acetonitrile (v/v) into 1.5 mL tubes and lysed in the
643 presence of 0.5mm Zirconia/silica beads by Bullet Blender (Next Advance) at 4 °C until the sample were
644 homogenized. The resulting lysate was then centrifuged at 21,000 x g for 5 min and the supernatant was
645 dried by speedvac. The samples were resuspended in 50 µL of 1% acetonitrile plus 0.1% trifluoroacetic
646 acid, and separated by Ultra-C18 Micro spin columns (Harvard apparatus) into hydrophilic metabolites
647 (flow through) and hydrophobic metabolites (eluent of 125 µL of 80% acetonitrile plus 0.1%
648 trifluoroacetic acid). Ten µL of hydrophilic metabolites were dried, reconstituted in 3 µL of 66%
649 acetonitrile and analyzed by a ZIC-HILIC column (150 × 2.1 mm, EMD Millipore) coupled with a Q
650 Exactive HF Orbitrap MS (Thermo Fisher) in negative mode and metabolites were eluted within a 45 min
651 gradient (buffer A: 10mM ammonium acetate in 90% acetonitrile (pH=8); buffer B: 10mM ammonium
652 acetate in 100% H_2O (pH=8)). Twenty µL of hydrophobic metabolites were dried and resuspend in 3 µL
653 of 5% formic acid followed by separation with a self-packed nanoC18 column (75 µm × 15 cm with 1.9
654 µm C18 resin from Dr. Maisch GmbH) and detection with a Q Exactive HF Orbitrap MS (Thermo Fisher)
655 in positive mode. Metabolites were eluted within a 50 min gradient (buffer A: 0.2% formic acid in H_2O;
656 buffer B: 0.2% formic acid in acetonitrile). MS settings for both types of samples included MS1 scans
657 (120,000 resolution, 100-1000 *m/z*, 3 x 10^6 AGC and 50 ms maximal ion time) and 20 data-dependent

658 MS2 scans (30,000 resolution, 2 x 10^5 AGC, ~45 ms maximal ion time, HCD, Stepped NCE (50, 100,
659 150), and 20 s dynamic exclusion). A mix of all samples served as quality control was injected in the
660 beginning, middle and the end of the samples to monitor the signal stability of the instrument. The data
661 analysis was performed by a recently developed software suite JUMPm. Raw files were converted to
662 mzXML format followed by peak feature detection for individual sample and feature alignment across
663 samples. Metabolite identification was supported by matching the retention time, accurate mass/charge
664 (m/z) ratio, and MS/MS fragmentation data to our in-house authentic compound library and the matching
665 of m/z and MS/MS fragmentation data to, downloaded experimental MS/MS library (MoNA,
666 https://mona.fiehnlab.ucdavis.edu/), in-silico database generated from Human Metabolome Database
667 (HMDB), and mzCloud (https://mzcloud.org). Peak intensities were used for metabolite quantification.
668 The data was normalized by both cell numbers (before data collection) and trimmed median intensity of
669 all features across samples (post data collection).
670
671 **Differential gene expression and gene set enrichment analysis (GSEA) for RNA-seq experiments.**
672 Total RNA from cells and tumor tissues were performed using the RNeasy Mini Kit (Qiagen) according
673 to the manufacturer's instructions. Paired-end sequencing was performed using the High-Seq platform
674 with 100bp read length. Total stranded RNA sequencing data were processed by the internal AutoMapper
675 pipeline. Briefly the raw reads were firs trimmed (Trim-Galore version 0.60), mapped to human genome
676 assembly (GRCh38) (STAR v2.7) and then the gene level values were quantified (RSEM v1.31) based on
677 GENCODE annotation (v31). Low count genes were removed from analysis using a CPM cutoff
678 corresponding to a count of 10 reads and only confidently annotated (level 1 and 2 gene annotation) and
679 protein-coding genes are used for differential expression analysis. Normalization factors were generated
680 using the TMM method, counts were then transformed using voom and transformed counts were analyzed
681 using the lmFit and eBayes functions (R limma package version 3.42.2). The significantly up- and down-
682 regulated genes were defined by at least 2-fold changes and adjusted p-value < 0.05. Then gene set
683 enrichment analysis (GSEA) was carried out using gene-level log2 fold changes from differential
684 expression results against gene sets in the Molecular Signatures Database (MSigDB 6.2) (gsea2 version
685 2.2.3).
686
687 **RNA splicing analysis.** After mapping RNA-seq data, rMATS v4.1.0 was used for RNA alternative
688 splicing analysis by using the mapped BAM files as input. Specifically, five different kinds of alternative
689 splicing events were identified, i.e., skipped exon (SE), alternative 5'-splicing site (A5SS), alternative 3'-
690 splicing site (A3SS), mutually exclusive exon (MXE) and intron retention (RI). To keep consistent, the

691 same GTF annotation reference file for mapping was used for rMATS. For stranded RNA-seq data, the
692 argument "--libType fr-firststrand" was applied. To process reads with variable lengths, the argument "--
693 variable-read-length" was also used for rMATS. To select statistically significantly differential splicing
694 events, the following thresholds were used: FDR <0.05 and the absolute value of IncLevelDifference >
695 0.1. For visualization, the IGV Genome Browser was used to show the sashimi plots of splicing events.
696 To investigate the genome-wide correlations of differential splicing between two genotypes (e.g., shRNA
697 knockdown of JMJD6 and non-target shRNA in cells), we extracted splice junctions for all samples of
698 both genotypes of interest from the STAR[105] output files suffixed with "SJ.out.tab", which contain high
699 confidence collapsed splice junctions. Only those unique mapped reads crossing the junctions were
700 considered. By extracting the union of the unique junction positions, we constructed a unified junction-
701 read feature vector for each sample. Then, we normalized the junction-read vectors of each sample with
702 TMM method in "voom" and "limma" and R package, assuming a negative binomial distribution. Next,
703 we averaged the junction-read vectors for samples of the same genotype. The gene level expression was
704 estimated based on the canonical junctions from the most abundant isoforms estimated for each gene. The
705 fold changes of exon junctions significantly deviated from gene level changes were regarded as
706 differentially spliced junctions for between cell-line comparisons.
707
708 **Data mining**. *JMJD6, GAC and KGA* expression in tumor tissues were downloaded from R2
709 (https://portals.broadinstitute.org/ccle), Kocak dataset GSE45547 (649 samples) and Fischer dataset
710 GSE120572 (394 samples). In both datasets, the probe UKv4_A_23_P311616 represented *JMJD6*, the
711 probe UKv4_A_23_P308800 represented *GAC* and UKv4_A_23_P39766 represented *KGA*. *JMJD6*
712 expression data from the RNA-seq data of various pediatric cancer tissues were downloaded from St Jude
713 cloud (https://pecan.stjude.cloud/). The copy number alterations of *JMJD6* and the related Kaplan-Meier
714 analysis were downloaded from cBioportal (cbioportal.org). The data for correlation of metabolite
715 abundance and JMJD6 knockout effect were downloaded from DepMap (https://depmap.org/portal/).
716
717 **Pathway network analysis**. The 114 essential fitness genes to neuroblastoma cell survival identified
718 through genome-wide CRISPR/Cas9 library screen were uploaded into STRING program (https://string-
719 db.org) for network interaction analysis with confidence threshold 0.15. The resulting network was then
720 uploaded into Cytoscape program for presentation[106]. The clusters were grouped based on the biological
721 functions of each gene.
722

723 **Copy number analysis of JMJD6 and other genes encoding JmjC domain histone demethylases from**
724 **St Jude neuroblastoma cohort.** Somatic copy number alternations (SCNA) were determined by
725 CONSERTING (PMID: 25938371) for each pair of tumor and normal samples. The normalize read depth
726 ratio (log2 ratio) for the CNV segments with JmjC-domain containing proteins were extracted and used
727 for CNV heatmap generation (https://CRAN. R-project. org/package= pheatmap) and hierarchical
728 clustering of samples.
729
730 **Xenograft studies.** (**1**) shRNA-mediated JMJD6 knockdown. Neuroblastoma cells were transduced with
731 shRNA lentiviral particles targeting JMJD6. 48 hours later, 1 μg/ml of puromycin was added for selection
732 for additional 48 hours. Cancer cells ($5x10^6$) were mixed with Matrigel (1:1 ratio in volume) and
733 subcutaneously injected into the flank sites of NSG mice. (**2**) JMJD6 and MYC-mediated transformation.
734 After JoMa1 cells were transduced with GFP, JMJD6, MYCN and JMJD6/MYCN, 10^4 cells per group
735 were mixed with Matrigel (1:1 ratio in volume) and subcutaneously injected into the flank sites of NSG
736 mice. Mice were sacrificed when they reached the humane endpoint. Tumors were measured by using
737 electronic calipers, and volumes calculated as width π/6 xd3 where d is the mean of two diameters taken
738 at right angles.
739
740 **Statistical analysis**. All quantitative data are presented as mean ± SD. Unpaired Student's t test was
741 performed for comparison of two groups. Spearman correlation was used to assess the relationship
742 between two variables. Kaplan-Meier method was used to estimate the survival rate. Mann-Whitney rank
743 test (two-sided) was used to compare the tumor volume between two groups at every time point. P-values
744 across multiple time points were adjusted for multiple comparison using the Holm-SidaK method. $p<0.05$
745 was considered as statistically significant. All the statistical analyses, except where otherwise noted, were
746 performed using GraphPad Prism (v9).
747
748 **Data accessibility.** GEO accession number: GSE185867
749 To review GEO accession GSE185867:
750 Go
751 to https://nam11.safelinks.protection.outlook.com/?url=https%3A%2F%2Fwww.ncbi.nlm.nih.gov%2Fg
752 eo%2Fquery%2Facc.cgi%3Facc%3DGSE185867&data=04%7C01%7Cjun.yang2%40stjude.org%
753 7C56d8ac619531468173d608d98ea927d8%7C22340fa892264871b677d3b3e377af72%7C0%7C0%7C6
754 37697679446209542%7CUnknown%7CTWFpbGZsb3d8eyJWIjoiMC4wLjAwMDAiLCJQIjoiV2luMz
755 IiLCJBTiI6Ik1haWwiLCJXVCI6Mn0%3D%7C1000&sdata=XtZl1ttoOPBvfhwmX9uCcwVN1Yg

02qDsvcsHdJv58xw%3D&reserved=0

Enter token qzixwsoohbsxjij into the box

Acknowledgements. We thank the staff of the St. Jude Animal Resource Center and Hartwell Center for their dedication and expertise. The work was supported by American Cancer Society-Research Scholar (130421-RSG-17-071-01-TBG, J.Y.), National Cancer Institute (1R01CA229739-01, J.Y., R01CA266600, J.Y.). The work was also supported by the American Lebanese Syrian Associated Charities (ALSAC). The content is solely the responsibility of the authors and does not necessarily represent the official views of the National Institutes of Health.

Author contributions. C.J., W.Q., S.S., H.H., D.H.B. D.H performed experiments. G.W., H.J., T-C.C., D.F., J-H.C performed proteomic, genomic and RNA-seq analysis. S.M.S and S.M.P-M provided CRISPR knockout. R.W., K.F. provided key reagents. A.M.D, A.M., J.P., and J.Y. supervised the studies. J.Y conceived the project and wrote the manuscript with help from co-authors.

References

1 Hanahan, D. & Weinberg, R. A. Hallmarks of cancer: the next generation. *Cell* **144**, 646-674 (2011). https://doi.org:10.1016/j.cell.2011.02.013

2 Pavlova, N. N. & Thompson, C. B. The Emerging Hallmarks of Cancer Metabolism. *Cell Metab* **23**, 27-47 (2016). https://doi.org:10.1016/j.cmet.2015.12.006

3 Vazquez, A. *et al.* Cancer metabolism at a glance. *J Cell Sci* **129**, 3367-3373 (2016). https://doi.org:10.1242/jcs.181016

4 DeBerardinis, R. J. & Chandel, N. S. Fundamentals of cancer metabolism. *Sci Adv* **2**, e1600200 (2016). https://doi.org:10.1126/sciadv.1600200

5 Kalkat, M. *et al.* MYC Deregulation in Primary Human Cancers. *Genes (Basel)* **8** (2017). https://doi.org:10.3390/genes8060151

6 Stine, Z. E., Walton, Z. E., Altman, B. J., Hsieh, A. L. & Dang, C. V. MYC, Metabolism, and Cancer. *Cancer Discov* **5**, 1024-1039 (2015). https://doi.org:10.1158/2159-8290.CD-15-0507

7 Hsu, T. Y. *et al.* The spliceosome is a therapeutic vulnerability in MYC-driven cancer. *Nature* **525**, 384-388 (2015). https://doi.org:10.1038/nature14985

8 Hirsch, C. L. *et al.* Myc and SAGA rewire an alternative splicing network during early somatic cell reprogramming. *Genes Dev* **29**, 803-816 (2015). https://doi.org:10.1101/gad.255109.114

9 Koh, C. M. *et al.* MYC regulates the core pre-mRNA splicing machinery as an essential step in lymphomagenesis. *Nature* **523**, 96-100 (2015). https://doi.org:10.1038/nature14351

10 Phillips, J. W. *et al.* Pathway-guided analysis identifies Myc-dependent alternative pre-mRNA splicing in aggressive prostate cancers. *Proc Natl Acad Sci U S A* **117**, 5269-5279 (2020). https://doi.org:10.1073/pnas.1915975117

11 Anczukow, O. & Krainer, A. R. The spliceosome, a potential Achilles heel of MYC-driven tumors. *Genome Med* **7**, 107 (2015). https://doi.org:10.1186/s13073-015-0234-3

12 Zhang, S. *et al.* MYCN controls an alternative RNA splicing program in high-risk metastatic neuroblastoma. *Cancer Lett* **371**, 214-224 (2016). https://doi.org:10.1016/j.canlet.2015.11.045

797 13 Gustafson, W. C. & Weiss, W. A. Myc proteins as therapeutic targets. *Oncogene* **29**, 1249-1259
798 (2010). https://doi.org:10.1038/onc.2009.512
799 14 Weiss, W. A., Aldape, K., Mohapatra, G., Feuerstein, B. G. & Bishop, J. M. Targeted expression of
800 MYCN causes neuroblastoma in transgenic mice. *EMBO J* **16**, 2985-2995 (1997).
801 https://doi.org:10.1093/emboj/16.11.2985
802 15 Zhu, S. *et al.* Activated ALK collaborates with MYCN in neuroblastoma pathogenesis. *Cancer Cell*
803 **21**, 362-373 (2012). https://doi.org:10.1016/j.ccr.2012.02.010
804 16 Tao, L. *et al.* MYCN-driven fatty acid uptake is a metabolic vulnerability in neuroblastoma. *Nat*
805 *Commun* **13**, 3728 (2022). https://doi.org:10.1038/s41467-022-31331-2
806 17 Khan, A. *et al.* Targeting metabolic activity in high-risk neuroblastoma through Monocarboxylate
807 Transporter 1 (MCT1) inhibition. *Oncogene* **39**, 3555-3570 (2020). https://doi.org:10.1038/s41388-
808 020-1235-2
809 18 Gamble, L. D. *et al.* Inhibition of polyamine synthesis and uptake reduces tumor progression and
810 prolongs survival in mouse models of neuroblastoma. *Sci Transl Med* **11** (2019).
811 https://doi.org:10.1126/scitranslmed.aau1099
812 19 Xia, Y. *et al.* Metabolic Reprogramming by MYCN Confers Dependence on the Serine-Glycine-
813 One-Carbon Biosynthetic Pathway. *Cancer Res* **79**, 3837-3850 (2019).
814 https://doi.org:10.1158/0008-5472.CAN-18-3541
815 20 Wang, T. *et al.* MYCN drives glutaminolysis in neuroblastoma and confers sensitivity to an ROS
816 augmenting agent. *Cell Death Dis* **9**, 220 (2018). https://doi.org:10.1038/s41419-018-0295-5
817 21 Bansal, M., Gupta, A. & Ding, H. F. MYCN and Metabolic Reprogramming in Neuroblastoma.
818 *Cancers (Basel)* **14** (2022). https://doi.org:10.3390/cancers14174113
819 22 Olsen, T. K. *et al.* DHODH is an independent prognostic marker and potent therapeutic target in
820 neuroblastoma. *JCI Insight* **7** (2022). https://doi.org:10.1172/jci.insight.153836
821 23 Alborzinia, H. *et al.* MYCN mediates cysteine addiction and sensitizes neuroblastoma to
822 ferroptosis. *Nat Cancer* **3**, 471-485 (2022). https://doi.org:10.1038/s43018-022-00355-4
823 24 Guo, X., Chen, Q. R., Song, Y. K., Wei, J. S. & Khan, J. Exon array analysis reveals neuroblastoma
824 tumors have distinct alternative splicing patterns according to stage and MYCN amplification
825 status. *BMC Med Genomics* **4**, 35 (2011). https://doi.org:10.1186/1755-8794-4-35
826 25 Shi, Y. *et al.* Aberrant splicing in neuroblastoma generates RNA-fusion transcripts and provides
827 vulnerability to spliceosome inhibitors. *Nucleic Acids Res* (2021).
828 https://doi.org:10.1093/nar/gkab054
829 26 Shi, Y. *et al.* Aberrant splicing in neuroblastoma generates RNA-fusion transcripts and provides
830 vulnerability to spliceosome inhibitors. *Nucleic Acids Res* **49**, 2509-2521 (2021).
831 https://doi.org:10.1093/nar/gkab054
832 27 Singh, S. *et al.* Targeting the spliceosome through RBM39 degradation results in exceptional
833 responses in high-risk neuroblastoma models. *Sci Adv* **7**, eabj5405 (2021).
834 https://doi.org:10.1126/sciadv.abj5405
835 28 Nijhuis, A. *et al.* Indisulam targets RNA splicing and metabolism to serve as a therapeutic strategy
836 for high-risk neuroblastoma. *Nat Commun* **13**, 1380 (2022). https://doi.org:10.1038/s41467-022-
837 28907-3
838 29 Pugh, T. J. *et al.* The genetic landscape of high-risk neuroblastoma. *Nat Genet* **45**, 279-284 (2013).
839 https://doi.org:10.1038/ng.2529
840 30 Molenaar, J. J. *et al.* Sequencing of neuroblastoma identifies chromothripsis and defects in
841 neuritogenesis genes. *Nature* **483**, 589-593 (2012). https://doi.org:10.1038/nature10910
842 31 Hagenbuchner, J., Kiechl-Kohlendorfer, U., Obexer, P. & Ausserlechner, M. J. BIRC5/Survivin as a
843 target for glycolysis inhibition in high-stage neuroblastoma. *Oncogene* **35**, 2052-2061 (2016).
844 https://doi.org:10.1038/onc.2015.264
845 32 MacArthur, I. C. *et al.* Prohibitin promotes de-differentiation and is a potential therapeutic target in
846 neuroblastoma. *JCI Insight* **5** (2019). https://doi.org:10.1172/jci.insight.127130

847 33 Milosevic, J. *et al.* PPM1D Is a Therapeutic Target in Childhood Neural Tumors. *Cancers (Basel)*
848 **13** (2021). https://doi.org:10.3390/cancers13236042
849 34 Meitinger, F. *et al.* TRIM37 controls cancer-specific vulnerability to PLK4 inhibition. *Nature* **585**,
850 440-446 (2020). https://doi.org:10.1038/s41586-020-2710-1
851 35 Garcia-Lopez, J. *et al.* Large 1p36 Deletions Affecting Arid1a Locus Facilitate Mycn-Driven
852 Oncogenesis in Neuroblastoma. *Cell Rep* **30**, 454-464 e455 (2020).
853 https://doi.org:10.1016/j.celrep.2019.12.048
854 36 Henrich, K. O. *et al.* CAMTA1, a 1p36 tumor suppressor candidate, inhibits growth and activates
855 differentiation programs in neuroblastoma cells. *Cancer Res* **71**, 3142-3151 (2011).
856 https://doi.org:10.1158/0008-5472.CAN-10-3014
857 37 Liu, Z. *et al.* CASZ1, a candidate tumor-suppressor gene, suppresses neuroblastoma tumor growth
858 through reprogramming gene expression. *Cell Death Differ* **18**, 1174-1183 (2011).
859 https://doi.org:10.1038/cdd.2010.187
860 38 Laut, A. K. *et al.* CHD5 inhibits metastasis of neuroblastoma. *Oncogene* **41**, 622-633 (2022).
861 https://doi.org:10.1038/s41388-021-02081-0
862 39 Higashi, M. *et al.* Retinoic acid-induced CHD5 upregulation and neuronal differentiation of
863 neuroblastoma. *Mol Cancer* **14**, 150 (2015). https://doi.org:10.1186/s12943-015-0425-y
864 40 Fujita, T. *et al.* CHD5, a tumor suppressor gene deleted from 1p36.31 in neuroblastomas. *J Natl*
865 *Cancer Inst* **100**, 940-949 (2008). https://doi.org:10.1093/jnci/djn176
866 41 Fell, S. M. *et al.* Neuroblast differentiation during development and in neuroblastoma requires
867 KIF1Bbeta-mediated transport of TRKA. *Genes Dev* **31**, 1036-1053 (2017).
868 https://doi.org:10.1101/gad.297077.117
869 42 Li, S. *et al.* The 1p36 Tumor Suppressor KIF 1Bbeta Is Required for Calcineurin Activation,
870 Controlling Mitochondrial Fission and Apoptosis. *Dev Cell* **36**, 164-178 (2016).
871 https://doi.org:10.1016/j.devcel.2015.12.029
872 43 Chen, Z. X. *et al.* RNA helicase A is a downstream mediator of KIF1Bbeta tumor-suppressor
873 function in neuroblastoma. *Cancer Discov* **4**, 434-451 (2014). https://doi.org:10.1158/2159-
874 8290.CD-13-0362
875 44 Cole, K. A. *et al.* A functional screen identifies miR-34a as a candidate neuroblastoma tumor
876 suppressor gene. *Mol Cancer Res* **6**, 735-742 (2008). https://doi.org:10.1158/1541-7786.MCR-07-
877 2102
878 45 Yu, F. *et al.* RUNX3 interacts with MYCN and facilitates protein degradation in neuroblastoma.
879 *Oncogene* **33**, 2601-2609 (2014). https://doi.org:10.1038/onc.2013.221
880 46 Bown, N. *et al.* Gain of chromosome arm 17q and adverse outcome in patients with neuroblastoma.
881 *N Engl J Med* **340**, 1954-1961 (1999). https://doi.org:10.1056/NEJM199906243402504
882 47 Althoff, K. *et al.* A Cre-conditional MYCN-driven neuroblastoma mouse model as an improved
883 tool for preclinical studies. *Oncogene* **34**, 3357-3368 (2015). https://doi.org:10.1038/onc.2014.269
884 48 Bottger, A., Islam, M. S., Chowdhury, R., Schofield, C. J. & Wolf, A. The oxygenase Jmjd6--a case
885 study in conflicting assignments. *Biochem J* **468**, 191-202 (2015).
886 https://doi.org:10.1042/BJ20150278
887 49 Chang, B., Chen, Y., Zhao, Y. & Bruick, R. K. JMJD6 is a histone arginine demethylase. *Science*
888 **318**, 444-447 (2007). https://doi.org:10.1126/science.1145801
889 50 Webby, C. J. *et al.* Jmjd6 catalyses lysyl-hydroxylation of U2AF65, a protein associated with RNA
890 splicing. *Science* **325**, 90-93 (2009). https://doi.org:10.1126/science.1175865
891 51 Kwok, J., O'Shea, M., Hume, D. A. & Lengeling, A. Jmjd6, a JmjC Dioxygenase with Many
892 Interaction Partners and Pleiotropic Functions. *Front Genet* **8**, 32 (2017).
893 https://doi.org:10.3389/fgene.2017.00032
894 52 Vangimalla, S. S., Ganesan, M., Kharbanda, K. K. & Osna, N. A. Bifunctional Enzyme JMJD6
895 Contributes to Multiple Disease Pathogenesis: New Twist on the Old Story. *Biomolecules* **7** (2017).
896 https://doi.org:10.3390/biom7020041

53 Zhou, J. *et al.* An oncogenic JMJD6-DGAT1 axis tunes the epigenetic regulation of lipid droplet formation in clear cell renal cell carcinoma. *Mol Cell* **82**, 3030-3044 e3038 (2022). https://doi.org:10.1016/j.molcel.2022.06.003
54 Paschalis, A. *et al.* JMJD6 Is a Druggable Oxygenase That Regulates AR-V7 Expression in Prostate Cancer. *Cancer Res* **81**, 1087-1100 (2021). https://doi.org:10.1158/0008-5472.CAN-20-1807
55 Yang, J. *et al.* Targeting Histone Demethylases in MYC-Driven Neuroblastomas with Ciclopirox. *Cancer Res* **77**, 4626-4638 (2017). https://doi.org:10.1158/0008-5472.CAN-16-0826
56 Wong, M. *et al.* JMJD6 is a tumorigenic factor and therapeutic target in neuroblastoma. *Nat Commun* **10**, 3319 (2019). https://doi.org:10.1038/s41467-019-11132-w
57 Liu, W. *et al.* Brd4 and JMJD6-associated anti-pause enhancers in regulation of transcriptional pause release. *Cell* **155**, 1581-1595 (2013). https://doi.org:10.1016/j.cell.2013.10.056
58 Miller, T. E. *et al.* Transcription elongation factors represent in vivo cancer dependencies in glioblastoma. *Nature* **547**, 355-359 (2017). https://doi.org:10.1038/nature23000
59 Loven, J. *et al.* Selective inhibition of tumor oncogenes by disruption of super-enhancers. *Cell* **153**, 320-334 (2013). https://doi.org:10.1016/j.cell.2013.03.036
60 Chapuy, B. *et al.* Discovery and characterization of super-enhancer-associated dependencies in diffuse large B cell lymphoma. *Cancer Cell* **24**, 777-790 (2013). https://doi.org:10.1016/j.ccr.2013.11.003
61 Puissant, A. *et al.* Targeting MYCN in neuroblastoma by BET bromodomain inhibition. *Cancer Discov* **3**, 308-323 (2013). https://doi.org:10.1158/2159-8290.CD-12-0418
62 Wyce, A. *et al.* BET inhibition silences expression of MYCN and BCL2 and induces cytotoxicity in neuroblastoma tumor models. *PLoS One* **8**, e72967 (2013). https://doi.org:10.1371/journal.pone.0072967
63 Meyers, R. M. *et al.* Computational correction of copy number effect improves specificity of CRISPR-Cas9 essentiality screens in cancer cells. *Nat Genet* **49**, 1779-1784 (2017). https://doi.org:10.1038/ng.3984
64 Brodeur, G. M. & Bagatell, R. Mechanisms of neuroblastoma regression. *Nat Rev Clin Oncol* **11**, 704-713 (2014). https://doi.org:10.1038/nrclinonc.2014.168
65 Delmore, J. E. *et al.* BET bromodomain inhibition as a therapeutic strategy to target c-Myc. *Cell* **146**, 904-917 (2011). https://doi.org:10.1016/j.cell.2011.08.017
66 Liu, W. *et al.* Brd4 and JMJD6-associated anti-pause enhancers in regulation of transcriptional pause release. *Cell* **155**, 1581-1595 (2013). https://doi.org:10.1016/j.cell.2013.10.056
67 Wu, G. *et al.* Inhibition of SF3B1 by molecules targeting the spliceosome results in massive aberrant exon skipping. *RNA* **24**, 1056-1066 (2018). https://doi.org:10.1261/rna.065383.117
68 Dang, C. V. MYC, metabolism, cell growth, and tumorigenesis. *Cold Spring Harb Perspect Med* **3** (2013). https://doi.org:10.1101/cshperspect.a014217
69 Miller, D. M., Thomas, S. D., Islam, A., Muench, D. & Sedoris, K. c-Myc and cancer metabolism. *Clin Cancer Res* **18**, 5546-5553 (2012). https://doi.org:10.1158/1078-0432.CCR-12-0977
70 Gordan, J. D., Thompson, C. B. & Simon, M. C. HIF and c-Myc: sibling rivals for control of cancer cell metabolism and proliferation. *Cancer Cell* **12**, 108-113 (2007). https://doi.org:10.1016/j.ccr.2007.07.006
71 Wise, D. R. & Thompson, C. B. Glutamine addiction: a new therapeutic target in cancer. *Trends Biochem Sci* **35**, 427-433 (2010). https://doi.org:10.1016/j.tibs.2010.05.003
72 Porter, L. D., Ibrahim, H., Taylor, L. & Curthoys, N. P. Complexity and species variation of the kidney-type glutaminase gene. *Physiol Genomics* **9**, 157-166 (2002). https://doi.org:10.1152/physiolgenomics.00017.2002
73 Cassago, A. *et al.* Mitochondrial localization and structure-based phosphate activation mechanism of Glutaminase C with implications for cancer metabolism. *Proc Natl Acad Sci U S A* **109**, 1092-1097 (2012). https://doi.org:10.1073/pnas.1112495109

946 74 Wang, J. B. *et al.* Targeting mitochondrial glutaminase activity inhibits oncogenic transformation.
947 *Cancer Cell* **18**, 207-219 (2010). https://doi.org:10.1016/j.ccr.2010.08.009
948 75 Gao, P. *et al.* c-Myc suppression of miR-23a/b enhances mitochondrial glutaminase expression and
949 glutamine metabolism. *Nature* **458**, 762-765 (2009). https://doi.org:10.1038/nature07823
950 76 Wise, D. R. *et al.* Myc regulates a transcriptional program that stimulates mitochondrial
951 glutaminolysis and leads to glutamine addiction. *Proc Natl Acad Sci U S A* **105**, 18782-18787
952 (2008). https://doi.org:10.1073/pnas.0810199105
953 77 Yuneva, M., Zamboni, N., Oefner, P., Sachidanandam, R. & Lazebnik, Y. Deficiency in glutamine
954 but not glucose induces MYC-dependent apoptosis in human cells. *J Cell Biol* **178**, 93-105 (2007).
955 https://doi.org:10.1083/jcb.200703099
956 78 Masamha, C. P. *et al.* CFIm25 regulates glutaminase alternative terminal exon definition to
957 modulate miR-23 function. *RNA* **22**, 830-838 (2016). https://doi.org:10.1261/rna.055939.116
958 79 Yi, J. *et al.* JMJD6 and U2AF65 co-regulate alternative splicing in both JMJD6 enzymatic activity
959 dependent and independent manner. *Nucleic Acids Res* **45**, 3503-3518 (2017).
960 https://doi.org:10.1093/nar/gkw1144
961 80 Li, H. *et al.* The landscape of cancer cell line metabolism. *Nat Med* **25**, 850-860 (2019).
962 https://doi.org:10.1038/s41591-019-0404-8
963 81 David, C. J., Chen, M., Assanah, M., Canoll, P. & Manley, J. L. HnRNP proteins controlled by c-
964 Myc deregulate pyruvate kinase mRNA splicing in cancer. *Nature* **463**, 364-368 (2010).
965 https://doi.org:10.1038/nature08697
966 82 Rauch, J. *et al.* c-Myc regulates RNA splicing of the A-Raf kinase and its activation of the ERK
967 pathway. *Cancer Res* **71**, 4664-4674 (2011). https://doi.org:10.1158/0008-5472.CAN-10-4447
968 83 Ge, Y. *et al.* The splicing factor RBM25 controls MYC activity in acute myeloid leukemia. *Nat*
969 *Commun* **10**, 172 (2019). https://doi.org:10.1038/s41467-018-08076-y
970 84 Seton-Rogers, S. RNA splicing: MYC maintains high-fidelity splicing. *Nat Rev Cancer* **15**, 385
971 (2015). https://doi.org:10.1038/nrc3977
972 85 Matera, A. G. & Wang, Z. A day in the life of the spliceosome. *Nat Rev Mol Cell Biol* **15**, 108-121
973 (2014). https://doi.org:10.1038/nrm3742
974 86 Wahl, M. C., Will, C. L. & Luhrmann, R. The spliceosome: design principles of a dynamic RNP
975 machine. *Cell* **136**, 701-718 (2009). https://doi.org:10.1016/j.cell.2009.02.009
976 87 Pan, Q., Shai, O., Lee, L. J., Frey, B. J. & Blencowe, B. J. Deep surveying of alternative splicing
977 complexity in the human transcriptome by high-throughput sequencing. *Nat Genet* **40**, 1413-1415
978 (2008). https://doi.org:10.1038/ng.259
979 88 Wang, E. T. *et al.* Alternative isoform regulation in human tissue transcriptomes. *Nature* **456**, 470-
980 476 (2008). https://doi.org:10.1038/nature07509
981 89 Yang, X. *et al.* Widespread Expansion of Protein Interaction Capabilities by Alternative Splicing.
982 *Cell* **164**, 805-817 (2016). https://doi.org:10.1016/j.cell.2016.01.029
983 90 Liu, Y. *et al.* Impact of Alternative Splicing on the Human Proteome. *Cell Rep* **20**, 1229-1241
984 (2017). https://doi.org:10.1016/j.celrep.2017.07.025
985 91 Daemen, A. *et al.* Pan-Cancer Metabolic Signature Predicts Co-Dependency on Glutaminase and
986 De Novo Glutathione Synthesis Linked to a High-Mesenchymal Cell State. *Cell Metab* **28**, 383-399
987 e389 (2018). https://doi.org:10.1016/j.cmet.2018.06.003
988 92 Redis, R. S. *et al.* Allele-Specific Reprogramming of Cancer Metabolism by the Long Non-coding
989 RNA CCAT2. *Mol Cell* **61**, 520-534 (2016). https://doi.org:10.1016/j.molcel.2016.01.015
990 93 Gong, C. *et al.* Sequential inverse dysregulation of the RNA helicases DDX3X and DDX3Y
991 facilitates MYC-driven lymphomagenesis. *Mol Cell* (2021).
992 https://doi.org:10.1016/j.molcel.2021.07.041
993 94 Bosse, K. R. & Maris, J. M. Advances in the translational genomics of neuroblastoma: From
994 improving risk stratification and revealing novel biology to identifying actionable genomic
995 alterations. *Cancer* (2015). https://doi.org:10.1002/cncr.29706

95 Pinto, N. R. *et al.* Advances in Risk Classification and Treatment Strategies for Neuroblastoma. *J Clin Oncol* **33**, 3008-3017 (2015). https://doi.org:10.1200/JCO.2014.59.4648

96 Brodeur, G. M. Neuroblastoma: biological insights into a clinical enigma. *Nat Rev Cancer* **3**, 203-216 (2003). https://doi.org:10.1038/nrc1014

97 Maris, J. M., Hogarty, M. D., Bagatell, R. & Cohn, S. L. Neuroblastoma. *Lancet* **369**, 2106-2120 (2007). https://doi.org:10.1016/S0140-6736(07)60983-0

98 Cohn, S. L. *et al.* The International Neuroblastoma Risk Group (INRG) classification system: an INRG Task Force report. *J Clin Oncol* **27**, 289-297 (2009). https://doi.org:10.1200/jco.2008.16.6785

99 Suh, E. *et al.* Late mortality and chronic health conditions in long-term survivors of early-adolescent and young adult cancers: a retrospective cohort analysis from the Childhood Cancer Survivor Study. *Lancet Oncol* **21**, 421-435 (2020). https://doi.org:10.1016/S1470-2045(19)30800-9

100 Nathan, P. C. *et al.* Health-related quality of life in adult survivors of childhood Wilms tumor or neuroblastoma: A report from the childhood cancer survivor study. *Pediatr Blood Cancer* **49**, 704-715 (2007). https://doi.org:10.1002/pbc.20949

101 Brady, S. W. *et al.* Pan-neuroblastoma analysis reveals age- and signature-associated driver alterations. *Nat Commun* **11**, 5183 (2020). https://doi.org:10.1038/s41467-020-18987-4

102 Han, T. *et al.* Anticancer sulfonamides target splicing by inducing RBM39 degradation via recruitment to DCAF15. *Science* **356** (2017). https://doi.org:10.1126/science.aal3755

103 Xu, P., Duong, D. M. & Peng, J. Systematical optimization of reverse-phase chromatography for shotgun proteomics. *J Proteome Res* **8**, 3944-3950 (2009). https://doi.org:10.1021/pr900251d

104 Bai, B. *et al.* U1 small nuclear ribonucleoprotein complex and RNA splicing alterations in Alzheimer's disease. *Proc Natl Acad Sci U S A* **110**, 16562-16567 (2013). https://doi.org:10.1073/pnas.1310249110

105 Dobin, A. *et al.* STAR: ultrafast universal RNA-seq aligner. *Bioinformatics* **29**, 15-21 (2013). https://doi.org:10.1093/bioinformatics/bts635

106 Shannon, P. *et al.* Cytoscape: a software environment for integrated models of biomolecular interaction networks. *Genome Res* **13**, 2498-2504 (2003). https://doi.org:10.1101/gr.1239303

Figure Legends

1027

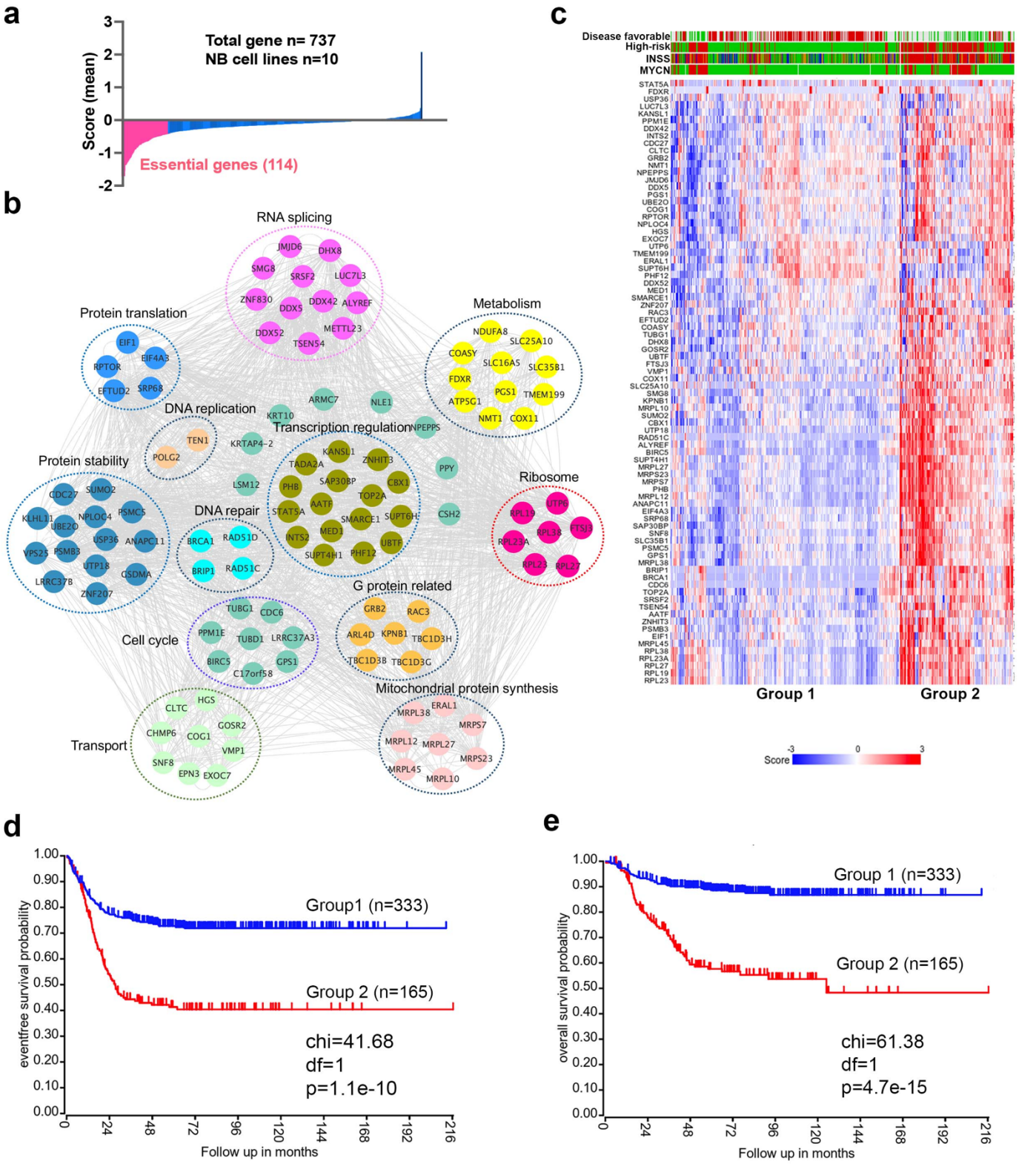

1028 **Figure 1. 17q contains neuroblastoma dependency genes**

1029 **a.** CRISPR score for 17q genes in 10 neuroblastoma cell lines. Score <-0.4 is defined as
1030 neuroblastoma dependency genes. Data are derived from Avana sgRNA library screening[63].
1031 **b.** STRING protein interaction network showing 17q essential genes with various biological
1032 functions.
1033 **c.** Heatmap by K-means clustering analysis showing 17q essential genes are highly expressed in
1034 high-risk neuroblastomas based on RNA-seq data (SEQC dataset).
1035 **d.** Kaplan-Meier survival curve showing 17q essential gene signature is correlated with worse
1036 event-free survival (SEQC dataset).
1037 **e.** Kaplan-Meier survival curve showing 17q essential gene signature is correlated with worse
1038 overall survival (SEQC dataset).

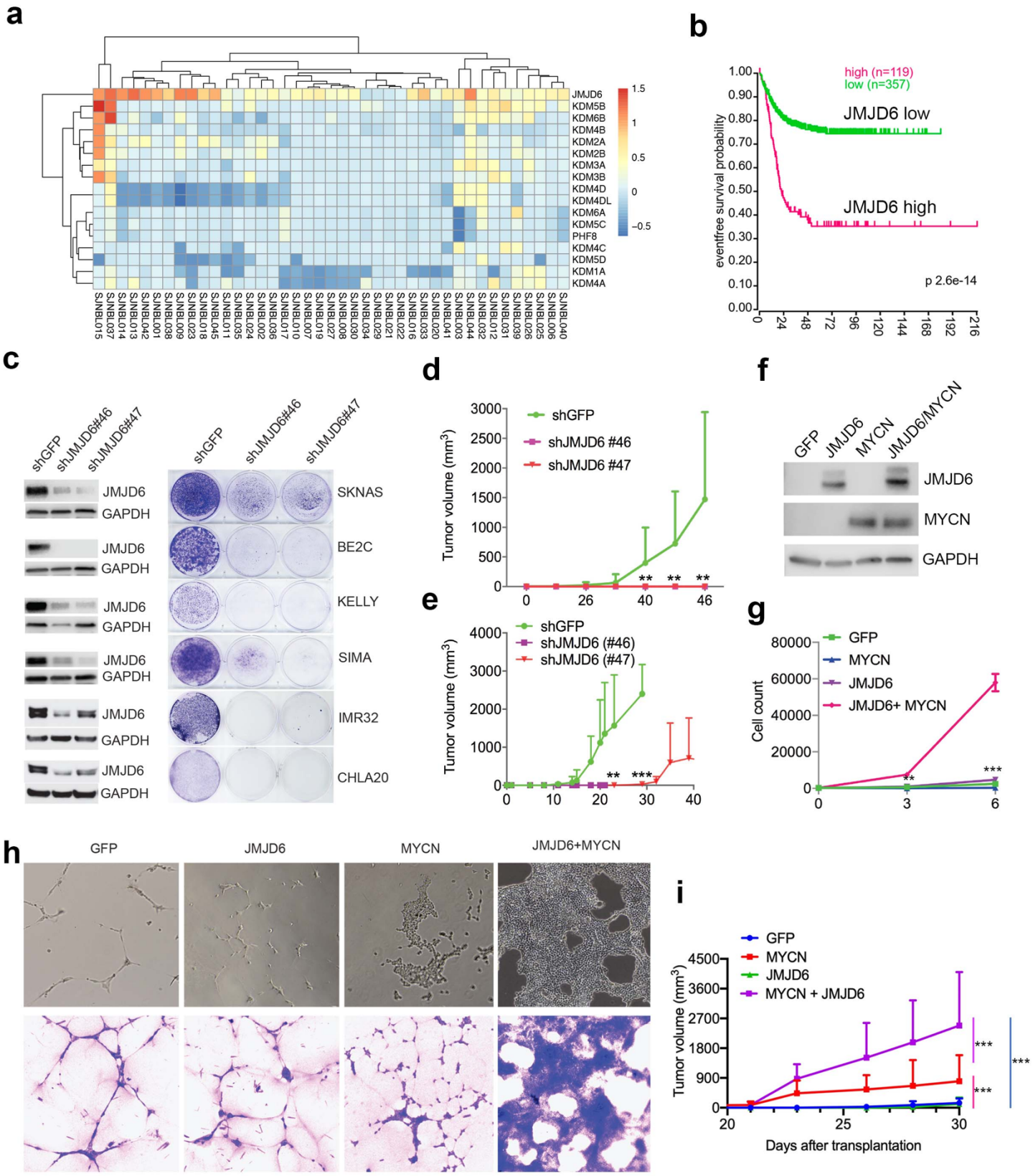
a
JMJD6
KDM5B
KDM6B
KDM4B
KDM2A
KDM2B
KDM3A
KDM3B
KDM4D
KDM4DL
KDM6A
KDM5C
PHF8
KDM4C
KDM5D
KDM1A
KDM4A
1.5
1
0.5
0
−0.5
b
high (n=119)
low (n=357)
JMJD6 low
JMJD6 high
eventfree survival probability
p 2.6e-14
c
shGFP
shJMJD6#46
shJMJD6#47
JMJD6
GAPDH
SKNAS
BE2C
KELLY
SIMA
IMR32
CHLA20
d
shGFP
shJMJD6 #46
shJMJD6 #47
Tumor volume (mm3)
e
shGFP
shJMJD6 (#46)
shJMJD6 (#47)
Tumor volume (mm3)
f
GFP
JMJD6
MYCN
JMJD6/MYCN
JMJD6
MYCN
GAPDH
g
GFP
MYCN
JMJD6
JMJD6+ MYCN
Cell count
h
GFP
JMJD6
MYCN
JMJD6+MYCN
i
GFP
MYCN
JMJD6
MYCN + JMJD6
Tumor volume (mm3)
Days after transplantation

1043 **Figure 2. JMJD6 is required for neuroblastoma growth and facilitates MYC-mediated cellular**
1044 **transformation.**

1045 **a.** Copy number of genes encoding JmjC domain proteins in St Jude neuroblastoma cohort.
1046 **b.** Kaplan-Meier survival curve showing high JMJD6 is correlated with worse event-free survival
1047 (SEQC RNA-seq dataset).
1048 **c.** Crystal violet showing the colony staining after JMJD6 siRNA knockdown in neuroblastoma cell
1049 lines validated by western blot.
1050 **d.** Xenograft tumor growth of BE2C (right) models with lentiviral JMJD6 shRNA knockdown. P-
1051 value calculated by multiple unpaired t-test across each row. n=5 per group.***p<0.001,
1052 **p<0.01.
1053 **e.** Xenograft tumor growth of SK-N-AS models with lentiviral JMJD6 shRNA knockdown. P- value
1054 calculated by multiple unpaired t-test across each row. ***p<0.001, **p<0.01.
1055 **f.** Western blot validating the expression of retroviral based MYCN and JMJD6 in JoMa1 cells.
1056 **g.** Cell proliferation of JoMa1 cells transduced with indicated constructs, GFP, JMJD6, MYCN,
1057 JMJD6+MYCN.
1058 **h.** Colony formation JoMa1 cells transduced with indicated constructs, GFP, JMJD6, MYCN,
1059 JMJD6+MYCN. Top panel showing photos taken under light microscope. Bottom panel showing
1060 cell colonies stained with crystal violet. P value calculated by multiple unpaired t-test across each
1061 row. ***p<0.001, **p<0.01.
1062 **i.** Xenograft tumor growth of JoMa1 cells transduced with indicated constructs, GFP, JMJD6, MYCN,
1063 JMJD6+MYCN. n=5 per group. P value calculated by multiple unpaired t-test across each row.
1064 ***p<0.001, **p<0.01.

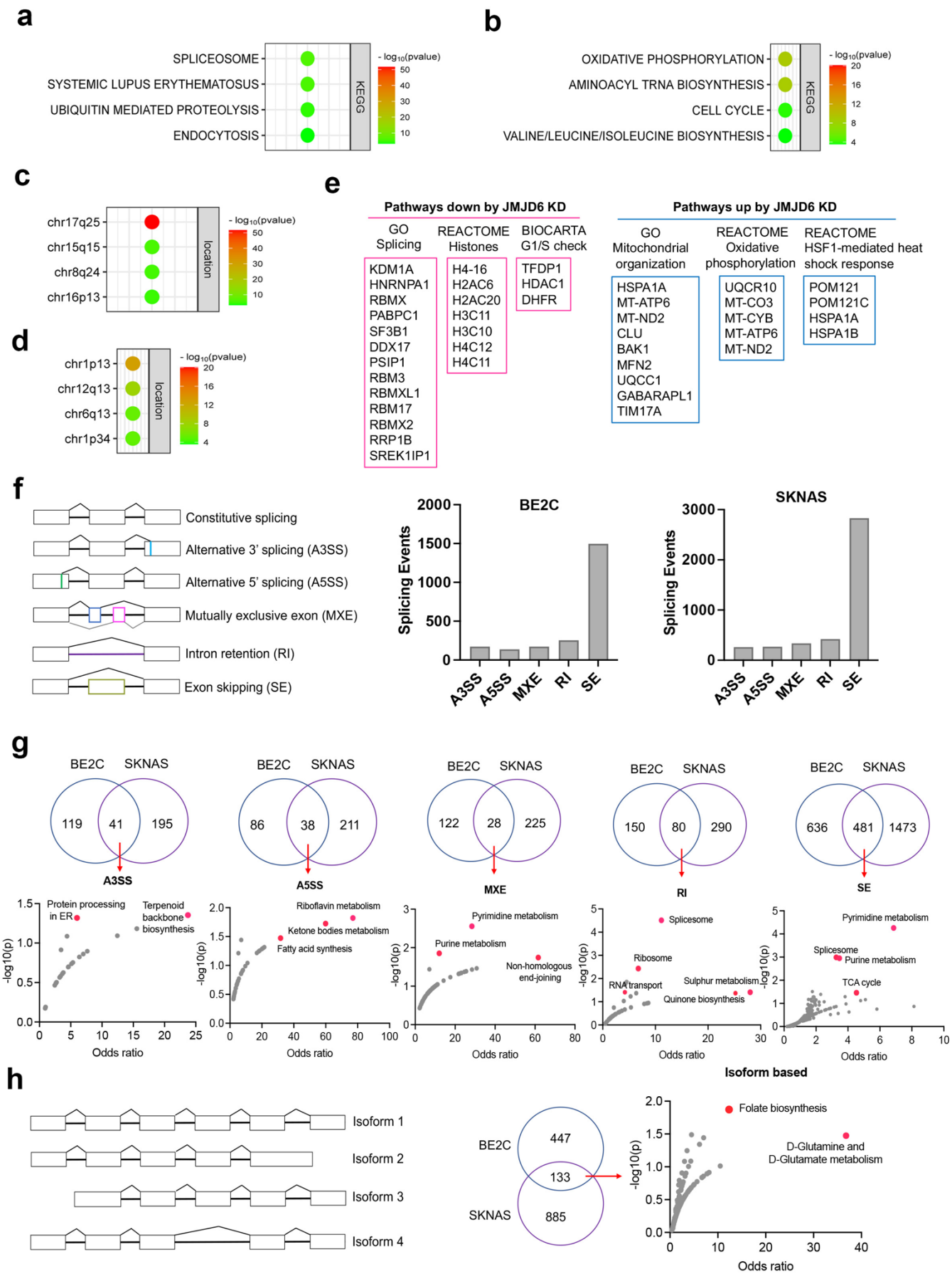
a
SPLICEOSOME
SYSTEMIC LUPUS ERYTHEMATOSUS
UBIQUITIN MEDIATED PROTEOLYSIS
ENDOCYTOSIS
KEGG
- log10(pvalue)
b
OXIDATIVE PHOSPHORYLATION
AMINOACYL TRNA BIOSYNTHESIS
CELL CYCLE
VALINE/LEUCINE/ISOLEUCINE BIOSYNTHESIS
c
chr17q25
chr15q15
chr8q24
chr16p13
location
d
chr1p13
chr12q13
chr6q13
chr1p34
e
Pathways down by JMJD6 KD
GO Splicing
KDM1A
HNRNPA1
RBMX
PABPC1
SF3B1
DDX17
PSIP1
RBM3
RBMXL1
RBM17
RBMX2
RRP1B
SREK1IP1
REACTOME Histones
H4-16
H2AC6
H2AC20
H3C11
H3C10
H4C12
H4C11
BIOCARTA G1/S check
TFDP1
HDAC1
DHFR
Pathways up by JMJD6 KD
GO Mitochondrial organization
HSPA1A
MT-ATP6
MT-ND2
CLU
BAK1
MFN2
UQCC1
GABARAPL1
TIM17A
REACTOME Oxidative phosphorylation
UQCR10
MT-CO3
MT-CYB
MT-ATP6
MT-ND2
REACTOME HSF1-mediated heat shock response
POM121
POM121C
HSPA1A
HSPA1B
f
Constitutive splicing
Alternative 3' splicing (A3SS)
Alternative 5' splicing (A5SS)
Mutually exclusive exon (MXE)
Intron retention (RI)
Exon skipping (SE)
BE2C
SKNAS
Splicing Events
A3SS
A5SS
MXE
RI
SE
g
BE2C
SKNAS
119
41
195
86
38
211
122
28
225
150
80
290
636
481
1473
Protein processing in ER
Terpenoid backbone biosynthesis
Riboflavin metabolism
Ketone bodies metabolism
Fatty acid synthesis
Pyrimidine metabolism
Purine metabolism
Non-homologous end-joining
Splicesome
Ribosome
RNA transport
Sulphur metabolism
Quinone biosynthesis
TCA cycle
-log10(p)
Odds ratio
Isoform based
h
Isoform 1
Isoform 2
Isoform 3
Isoform 4
447
133
885
Folate biosynthesis
D-Glutamine and D-Glutamate metabolism

1065 **Figure 3. JMJD6 regulates pre-mRNA splicing of genes involved in metabolism**

1066 **a.** Pathway enrichment for JMJD6 co-dependency genes whose knockout exhibits similar phenotype
1067 with JMJD6 knockout based on re-analysis of DepMAP data.

1068 **b.** Pathway enrichment for genes whose knockout exhibits opposite phenotype with JMJD6 knockout
1069 based on re-analysis of DepMAP data.

1070 **c.** Chromosomal location enrichment for JMJD6 co-dependency genes whose knockout exhibits
1071 similar phenotype with JMJD6 knockout based on re-analysis of DepMAP data.

1072 **d.** Chromosomal location enrichment for genes whose knockout exhibits opposite phenotype with
1073 JMJD6 knockout based on re-analysis of DepMAP data.

1074 **e.** Pathways analysis for genes downregulated and upregulated by JMJD6 knockdown commonly
1075 shared in SK-NAS and BE2C cells.

1076 **f.** Alternative splicing events altered by JMJD6 knockdown in BE2C and SK-N-AS cells.

1077 **g.** Pathway enrichment for each splicing event commonly shared in BE2C and SK-N-AS cells after
1078 JMJD6 knockdown.

1079 **h.** Isoform identification based on splicing events in BE2C and SK-N-AS cells, followed by pathway
1080 enrichment for commonly shared alterations in both cell lines.

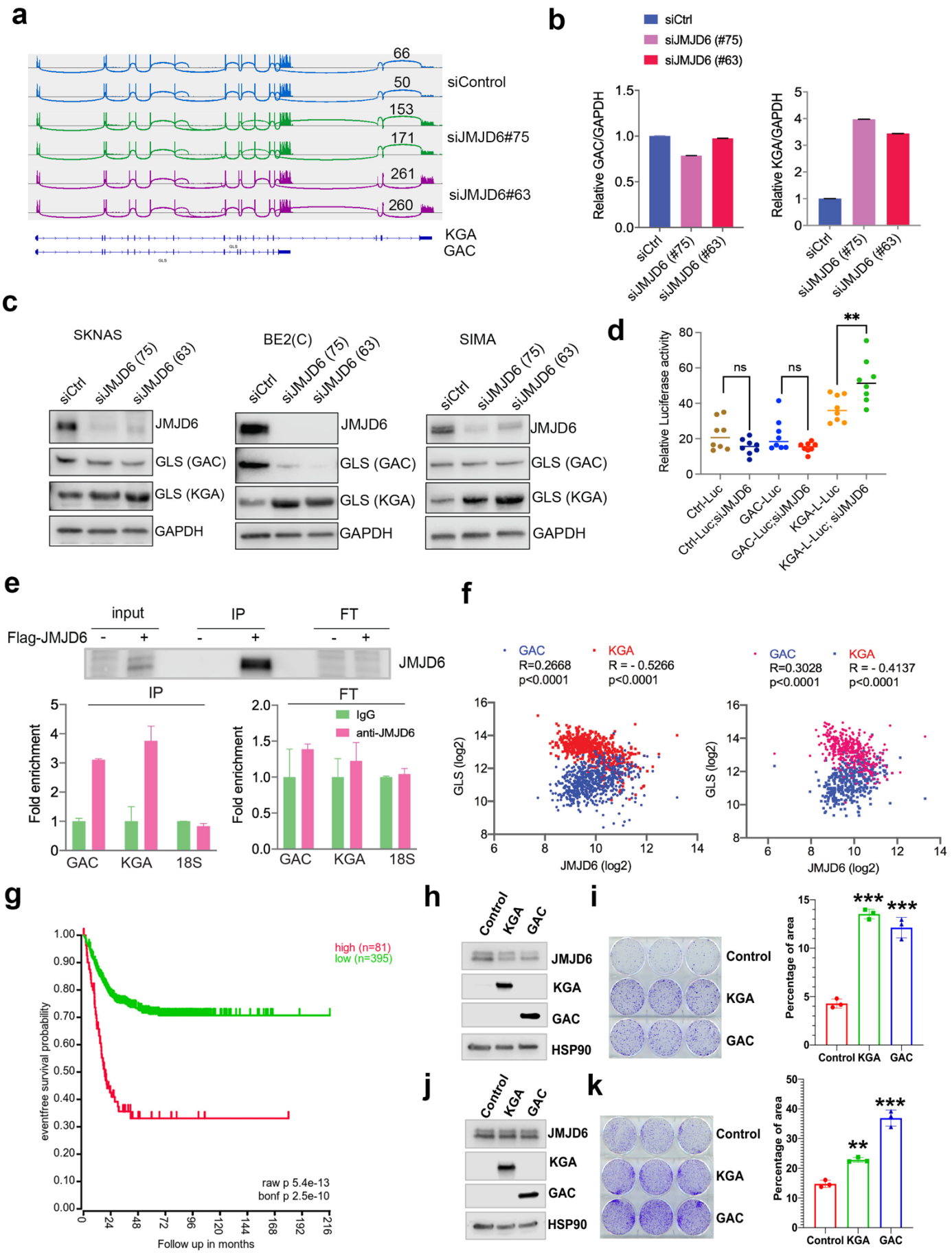
a
66
50
siControl
153
171
siJMJD6#75
261
siJMJD6#63
260
KGA
GAC
b
siCtrl
siJMJD6 (#75)
siJMJD6 (#63)
Relative GAC/GAPDH
Relative KGA/GAPDH
c
SKNAS
BE2(C)
SIMA
siCtrl
siJMJD6 (75)
siJMJD6 (63)
JMJD6
GLS (GAC)
GLS (KGA)
GAPDH
d
Relative Luciferase activity
ns
**
Ctrl-Luc
Ctrl-Luc;siJMJD6
GAC-Luc
GAC-Luc;siJMJD6
KGA-L-Luc
KGA-L-Luc; siJMJD6
e
input
IP
FT
Flag-JMJD6
JMJD6
Fold enrichment
IgG
anti-JMJD6
GAC
KGA
18S
f
GAC
KGA
R=0.2668
p<0.0001
R = - 0.5266
p<0.0001
R=0.3028
p<0.0001
R = - 0.4137
p<0.0001
GLS (log2)
JMJD6 (log2)
g
high (n=81)
low (n=395)
eventfree survival probability
raw p 5.4e-13
bonf p 2.5e-10
Follow up in months
h
Control
KGA
GAC
JMJD6
HSP90
i
Percentage of area
***
j
k
**

1081

1082 **Figure 4. JMJD6 regulates alternative splicing of glutaminolysis gene, GLS**

1083 **a.** Sashimi plot showing the alternative splicing of *GLS* after JMJD6 knockdown in BE2C and SK-
1084 N-AS cells in duplicates. The number indicates the RNA-seq read counts of exon junction.

1085 **b.** Real time PCR assessing the relative expression of *GAC* and *KGA* isoforms after JMJD6
1086 knockdown in triplicates.

1087 **c.** Western blot showing the expression of GAC and KGA isoforms in SK-N-AS, BE2C, SIMA
1088 after JMJD6 knockdown for 72 hours.

1089 **d.** KGA and GAC specific reporter analysis showing only KGA-driven luciferase activity is
1090 significantly upregulated by JMJD6 knockdown.

1091 **e.** RNA-immunoprecipitation showing JMJD6 interaction with *GLS* RNA. Top panel shows the
1092 western blot analysis of Flag tagged JMJD6 in input, immunoprecipitation (IP) and flowthrough
1093 (FT)_fractions. Bottom panel shows RT PCR analysis of enrichment of GAC/KGA bound by
1094 JMJD6 in IP and FT fractions.

1095 **f.** Spearman correlation analysis of *JMJD6* and *GAC*/*KGA* expression levels in two neuroblastoma
1096 cohorts GSE45547(left) and GSE120572 (right).

1097 **g.** Kaplan-Meier curve showing the association of *GAC* and *KGA* expression levels with event-free
1098 survival in a cohort of neuroblastoma (GSE45547).

1099 **h.** Western blotting analysis of expression of KGA and GAC in BE2C cells with indicated
1100 antibodies.

1101 **i.** Colony formation assay for BE2C cells overexpressing KGA and GAC for 7 days (left =crystal
1102 violet staining, right = quantification of cell density). **$p<0.001$,

1103 **j.** Western blotting analysis of expression of KGA and GAC in SK-N-AS cells with indicated
1104 antibodies.

1105 **k.** Colony formation assay for SK-N-AS cells overexpressing KGA and GAC for 7 days (left
1106 =crystal violet staining, right = quantification of cell density). **$p<0.001$,

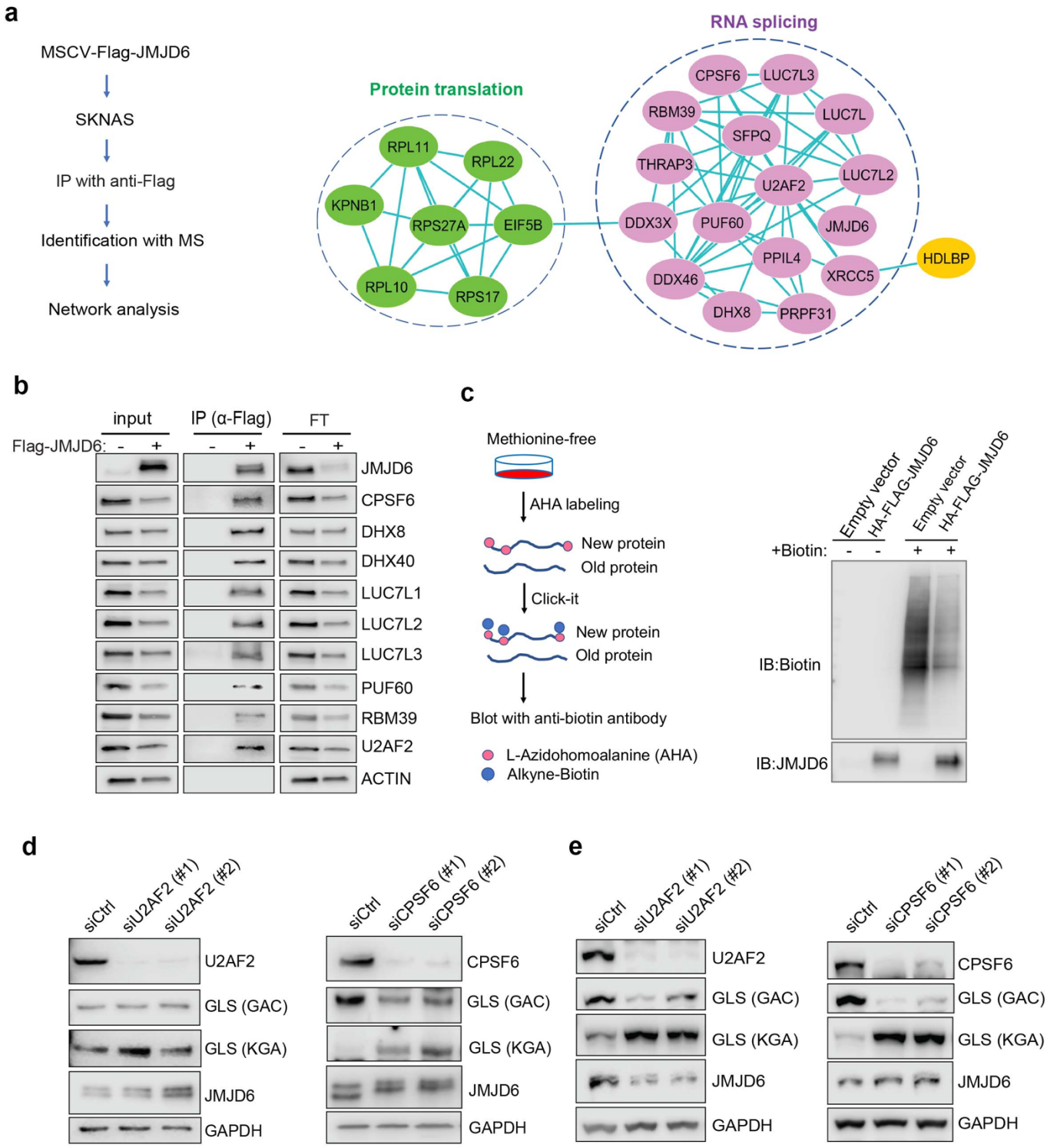
a
MSCV-Flag-JMJD6
SKNAS
IP with anti-Flag
Identification with MS
Network analysis
Protein translation
RPL11
RPL22
KPNB1
RPS27A
EIF5B
RPL10
RPS17
RNA splicing
CPSF6
LUC7L3
RBM39
LUC7L
SFPQ
THRAP3
U2AF2
LUC7L2
DDX3X
PUF60
JMJD6
PPIL4
HDLBP
DDX46
XRCC5
DHX8
PRPF31
b
input
IP (α-Flag)
FT
Flag-JMJD6: - + - + - +
JMJD6
CPSF6
DHX8
DHX40
LUC7L1
LUC7L2
LUC7L3
PUF60
RBM39
U2AF2
ACTIN
c
Methionine-free
AHA labeling
New protein
Old protein
Click-it
New protein
Old protein
Blot with anti-biotin antibody
L-Azidohomoalanine (AHA)
Alkyne-Biotin
Empty vector
HA-FLAG-JMJD6
Empty vector
HA-FLAG-JMJD6
+Biotin: - - + +
IB:Biotin
IB:JMJD6
d
siCtrl
siU2AF2 (#1)
siU2AF2 (#2)
U2AF2
GLS (GAC)
GLS (KGA)
JMJD6
GAPDH
siCtrl
siCPSF6 (#1)
siCPSF6 (#2)
CPSF6
GLS (GAC)
GLS (KGA)
JMJD6
GAPDH
e
siCtrl
siU2AF2 (#1)
siU2AF2 (#2)
U2AF2
GLS (GAC)
GLS (KGA)
JMJD6
GAPDH
siCtrl
siCPSF6 (#1)
siCPSF6 (#2)
CPSF6
GLS (GAC)
GLS (KGA)
JMJD6
GAPDH

1107

1108 **Figure 5. JMJD6 forms an interaction network consists of proteins involved in splicing and protein**
1109 **synthesis**

1110 **a.** Flag tagged JMJD6 transduced into SK-N-AS cells for immunoprecipitation with anti-Flag
1111 followed by protein identification by mass spectrometry. The interacting protein partners of
1112 JMJD6 are analyzed by STRING protein network.

1113 **b.** Immunoprecipitation followed by western blot to validate the JMJD6 interacting partners in
1114 SK-N-AS cells. IP= immunoprecipitation, FT= flowthrough.

1115 **c.** Click-IT AHA labeling showing the newly synthesized proteins after overexpression of
1116 JMJD6 in SK-N-AS cells.

1117 **d,e.** Western blot showing the expression of GAC and KGA isoforms in BE2C (d) SK-N-AS (e),
1118 after U2AF2 and CPSF6 knockdown for 72hours.

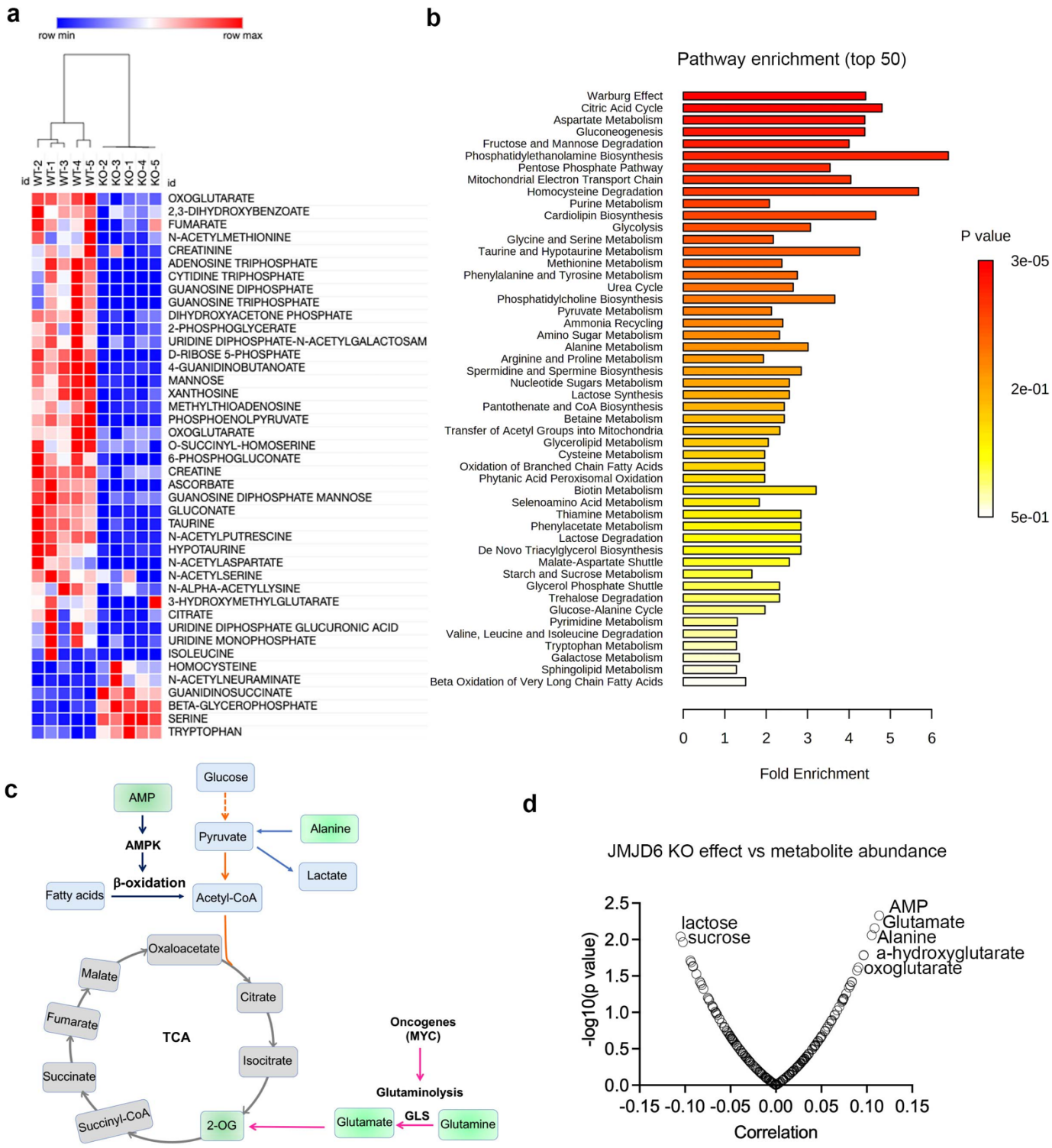
a
row min
row max
id
WT-2
WT-1
WT-3
WT-4
WT-5
KO-2
KO-3
KO-1
KO-4
KO-5
OXOGLUTARATE
2,3-DIHYDROXYBENZOATE
FUMARATE
N-ACETYLMETHIONINE
CREATININE
ADENOSINE TRIPHOSPHATE
CYTIDINE TRIPHOSPHATE
GUANOSINE DIPHOSPHATE
GUANOSINE TRIPHOSPHATE
DIHYDROXYACETONE PHOSPHATE
2-PHOSPHOGLYCERATE
URIDINE DIPHOSPHATE-N-ACETYLGALACTOSAM
D-RIBOSE 5-PHOSPHATE
4-GUANIDINOBUTANOATE
MANNOSE
XANTHOSINE
METHYLTHIOADENOSINE
PHOSPHOENOLPYRUVATE
OXOGLUTARATE
O-SUCCINYL-HOMOSERINE
6-PHOSPHOGLUCONATE
CREATINE
ASCORBATE
GUANOSINE DIPHOSPHATE MANNOSE
GLUCONATE
TAURINE
N-ACETYLPUTRESCINE
HYPOTAURINE
N-ACETYLASPARTATE
N-ACETYLSERINE
N-ALPHA-ACETYLLYSINE
3-HYDROXYMETHYLGLUTARATE
CITRATE
URIDINE DIPHOSPHATE GLUCURONIC ACID
URIDINE MONOPHOSPHATE
ISOLEUCINE
HOMOCYSTEINE
N-ACETYLNEURAMINATE
GUANIDINOSUCCINATE
BETA-GLYCEROPHOSPHATE
SERINE
TRYPTOPHAN
b
Pathway enrichment (top 50)
Warburg Effect
Citric Acid Cycle
Aspartate Metabolism
Gluconeogenesis
Fructose and Mannose Degradation
Phosphatidylethanolamine Biosynthesis
Pentose Phosphate Pathway
Mitochondrial Electron Transport Chain
Homocysteine Degradation
Purine Metabolism
Cardiolipin Biosynthesis
Glycolysis
Glycine and Serine Metabolism
Taurine and Hypotaurine Metabolism
Methionine Metabolism
Phenylalanine and Tyrosine Metabolism
Urea Cycle
Phosphatidylcholine Biosynthesis
Pyruvate Metabolism
Ammonia Recycling
Amino Sugar Metabolism
Alanine Metabolism
Arginine and Proline Metabolism
Spermidine and Spermine Biosynthesis
Nucleotide Sugars Metabolism
Lactose Synthesis
Pantothenate and CoA Biosynthesis
Betaine Metabolism
Transfer of Acetyl Groups into Mitochondria
Glycerolipid Metabolism
Cysteine Metabolism
Oxidation of Branched Chain Fatty Acids
Phytanic Acid Peroxisomal Oxidation
Biotin Metabolism
Selenoamino Acid Metabolism
Thiamine Metabolism
Phenylacetate Metabolism
Lactose Degradation
De Novo Triacylglycerol Biosynthesis
Malate-Aspartate Shuttle
Starch and Sucrose Metabolism
Glycerol Phosphate Shuttle
Trehalose Degradation
Glucose-Alanine Cycle
Pyrimidine Metabolism
Valine, Leucine and Isoleucine Degradation
Tryptophan Metabolism
Galactose Metabolism
Sphingolipid Metabolism
Beta Oxidation of Very Long Chain Fatty Acids
P value
3e-05
2e-01
5e-01
0
1
2
3
4
5
6
Fold Enrichment
c
Glucose
AMP
AMPK
Pyruvate
Alanine
Lactate
β-oxidation
Fatty acids
Acetyl-CoA
Oxaloacetate
Malate
Citrate
Fumarate
TCA
Isocitrate
Succinate
Succinyl-CoA
2-OG
Oncogenes
(MYC)
Glutaminolysis
Glutamate
GLS
Glutamine
d
JMJD6 KO effect vs metabolite abundance
lactose
sucrose
AMP
Glutamate
Alanine
a-hydroxyglutarate
oxoglutarate
-log10(p value)
2.5
2.0
1.5
1.0
0.5
0.0
-0.15
-0.10
-0.05
0.00
0.05
0.10
0.15
Correlation

1119

1120 **Figure 6. JMJD6 regulates production of citric acid cycle intermediates and NTP**

1121 **a.** Heatmap showing the metabolites differentially expressed in SK-N-AS cells (n=5) after
1122 JMJD6 knockout (n=5) based on LC-MS/MS analysis.

1123 **b.** Pathway analysis of metabolites downregulated by JMJD6 knockout.

1124 **c.** Pathway cartoon showing the connections of TCA, glycolysis, glutaminolysis, and β-
1125 oxidation.

1126 **d.** Correlation of metabolite abundance with JMJD6 dependency. The positive correlation
1127 indicates that the higher the abundance of metabolites, the more resistance of cells to JMJD6
1128 knockout. On the contrary, the negative correlation indicates the higher the abundance of
1129 metabolites, the more sensitive of cells to JMJD6 knockout.

1130

1131

1132

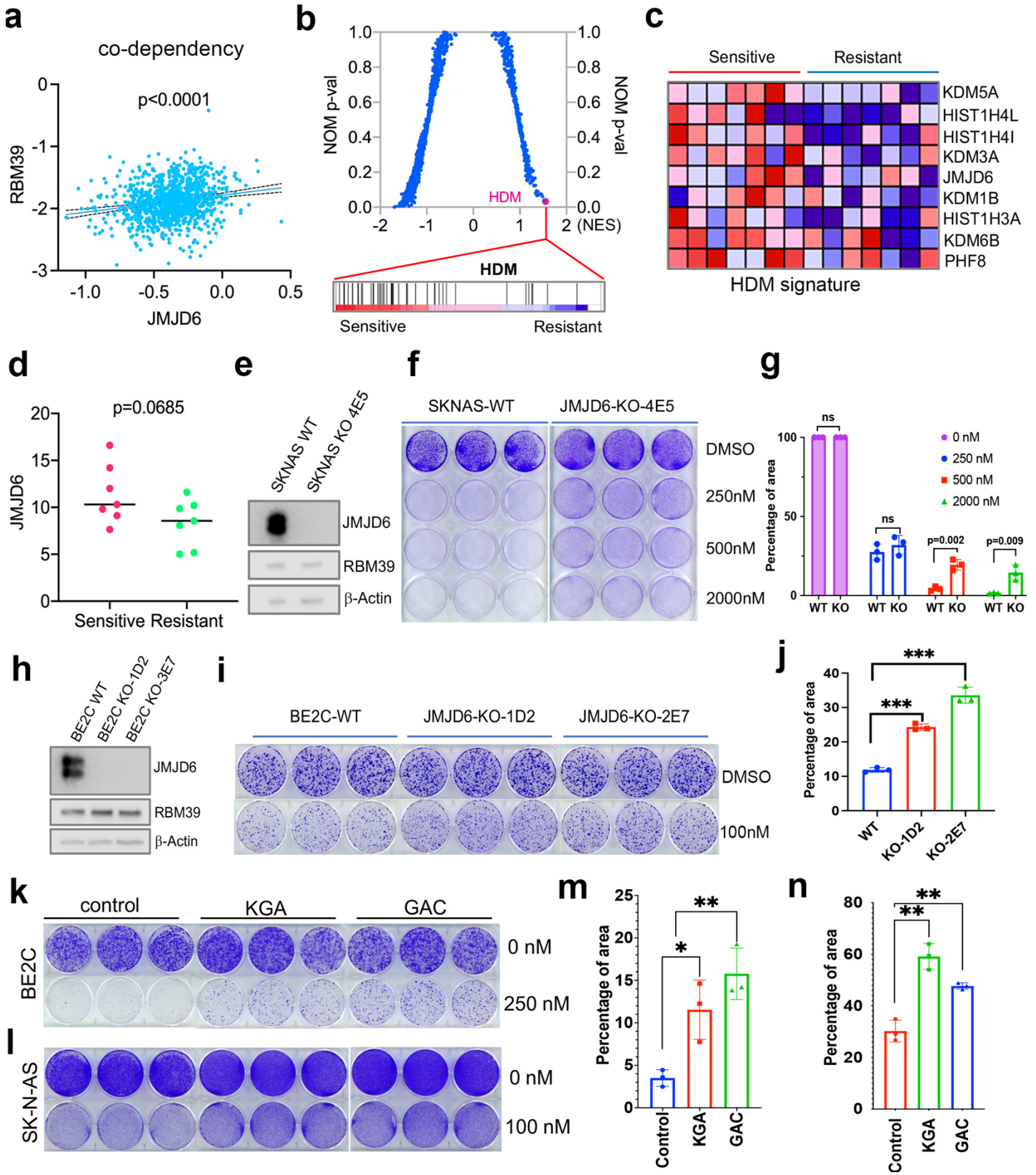
a
co-dependency
p<0.0001
RBM39
JMJD6
b
NOM p-val
HDM
2 (NES)
HDM
Sensitive
Resistant
c
Sensitive
Resistant
KDM5A
HIST1H4L
HIST1H4I
KDM3A
JMJD6
KDM1B
HIST1H3A
KDM6B
PHF8
HDM signature
d
p=0.0685
JMJD6
Sensitive Resistant
e
SKNAS WT
SKNAS KO 4E5
JMJD6
RBM39
β-Actin
f
SKNAS-WT
JMJD6-KO-4E5
DMSO
250nM
500nM
2000nM
g
Percentage of area
ns
p=0.002
p=0.009
0 nM
250 nM
500 nM
2000 nM
WT KO
h
BE2C WT
BE2C KO-1D2
BE2C KO-3E7
JMJD6
RBM39
β-Actin
i
BE2C-WT
JMJD6-KO-1D2
JMJD6-KO-2E7
DMSO
100nM
j
Percentage of area
***
WT
KO-1D2
KO-2E7
k
control
KGA
GAC
BE2C
0 nM
250 nM
l
SK-N-AS
0 nM
100 nM
m
Percentage of area
**
*
Control
KGA
GAC
n
Percentage of area
**
**
Control
KGA
GAC

1137 **Figure 7. JMJD6-GAC pathway regulates the response of neuroblastoma cells to indisulam treatment**

1138 **a.** Spearman correlation of effects of JMJD6 knockout and RBM39 knockout demonstrating the
1139 co-dependency of JMJD6 and RBM39 from DepMAP CRISPR screening data (n=1086). Each
1140 dot represents one cell line.

1141 **b.** GSEA analysis for indisulam sensitive vs resistant neuroblastoma cell lines based on CTD2
1142 (Cancer Target Discovery and Development) data showing histone lysine demethylase gene
1143 signature is the one that is significantly associated with indisulam response.

1144 **c.** Heatmap from GSEA (b) showing the individual genes in indisulam sensitive and resistant cells.

1145 **d.** JMJD6 expression in indisulam sensitive and resistant neuroblastoma cells. p value calculated
1146 by student t test.

1147 **e.** Western blot showing JMJD6 knockout in SK-N-AS cells using indicated antibodies.

1148 **f.** Colony formation of SK-N-AS cells in triplicates with or without JMJD6 knockout treated with
1149 different concentrations of indisulam for 7 days, stained with crystal violet.

1150 **g.** Quantification of cell density by using Image J from f. ns=not significant. ** $p<0.001$,
1151 ***$p<0.0001$

1152 **h.** Western blot showing JMJD6 knockout in BE2C cells using indicated antibodies.

1153 **i.** Colony formation of BE2C cells in triplicates with or without JMJD6 knockout treated with
1154 100nM of indisulam for 5 days, stained with crystal violet.

1155 **j.** Quantification of cell density by using Image J from f. ns=not significant. ** $p<0.001$,
1156 ***$p<0.0001$

1157 **k.** Colony formation of BE2C cells in triplicates with KGA and GAC overexpression treated with
1158 250nM of indisulam for 5 days, stained with crystal violet.

1159 **l.** Colony formation of SK-N-AS cells in triplicates with KGA and GAC overexpression treated
1160 with 100nM of indisulam for 7 days, stained with crystal violet.

1161 **m.** Quantification of cell density by using Image k from k. * $p<0.01$, **$p<0.001$

1162 **n.** Quantification of cell density by using Image l from k. **$p<0.001$

1163

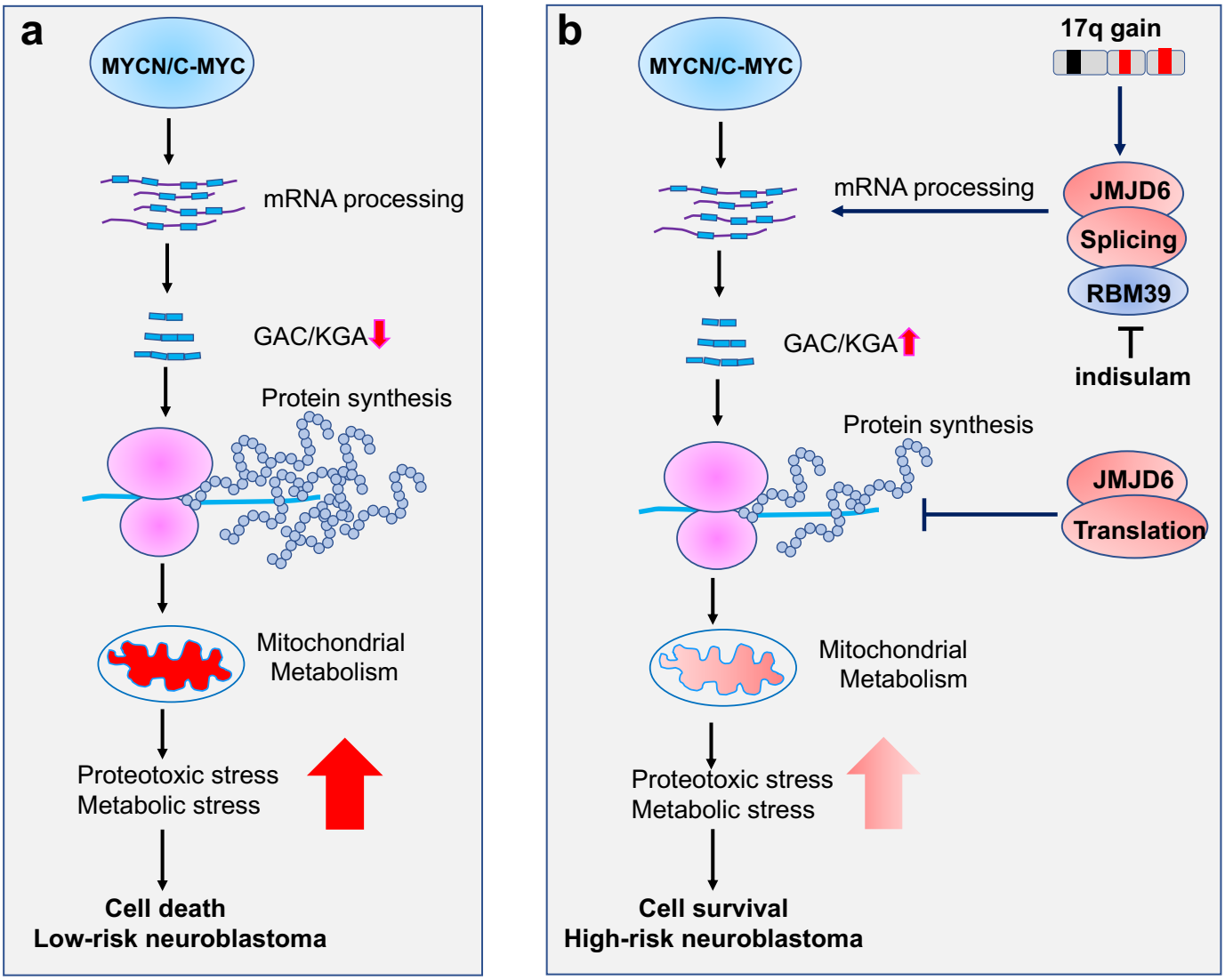

Figure 8. Working mechanism of JMJD6 in MYC-driven neuroblastoma. Overactive MYC drives high-load of gene transcription, enhanced protein synthesis and high rate of metabolism, leading to detrimental cellular stresses and consequent cell death (**Model a**). However, when 17q is amplified, high levels of JMJD6 and other proteins encoded by 17q genes physically interacts with the splicing and translational machineries, enhancing pre-mRNA splicing of metabolic genes such as GLS and inhibiting global protein synthesis, respectively, leading to reduced detrimental stresses and enhanced cancer cell survival and tumorigenesis (**Model b**). The high levels of JMJD6 predicts high dependency of RBM39, which are more sensitive to indisulam treatment.